

# Bondi-Hoyle-Lyttleton Accretion around the Rotating Hairy Horndeski Black Hole

---

**O. Donmez**

*College of Engineering and Technology, American University of the Middle East, Egaila 54200, Kuwait*

*E-mail: [orhan.donmez@aum.edu.kw](mailto:orhan.donmez@aum.edu.kw)*

**ABSTRACT:** Modeling of the shock cone formed around a stationary, hairy Horndeski black hole with Bondi-Hoyle-Lyttleton (BHL) accretion has been conducted. We model the dynamical changes of the shock cone resulting from the interaction of matter with the Horndeski black hole, where the scalar field and spacetime have a strong interaction. The effects of the scalar hair, the black hole rotation parameter, and the impacts of the asymptotic speed have been examined, revealing the influence of these parameters on the shock cone and the trapped QPO modes within the cone. Numerical calculations have shown that the hair parameter significantly affects the formation of the shock cone. As the absolute value of the hair parameter increases, the matter in the region of the shock cone is observed to move away from the black hole horizon. The rate of matter expulsion increases as  $h/M$  changes. After  $h/M < -0.6$ , a visible change in the physical structure of the shock cone occurs, ultimately leading to the complete removal out of the shock cone. On the other hand, it has been revealed that the asymptotic speed significantly affects the formation of the shock cone. As  $h/M$  increases in the negative direction and the asymptotic speed increases, the stagnation point moves closer to the black hole horizon. When the value of the hair parameter changes, the rest-mass density of the matter inside the cone decreases, whereas the opposite is observed with the asymptotic speed. Additionally, the formed shock cone has excited QPO modes. The deformation of the cone due to the hair parameter has led to a change or complete disappearance of the QPOs. Meanwhile, at asymptotic speeds of  $V_\infty/c < 0.4$ , all fundamental frequency modes are formed, while at  $V_\infty/c = 0.4$ , only the azimuthal mode is excited, and  $1 : 2 : 3 : 4 : \dots$  resonance conditions occur. No QPOs have formed at  $V_\infty/c = 0.6$ . The results obtained from numerical calculations have been compared with theoretical studies for  $M87^*$ , and it has been observed that the possible values of  $h/M$  found in the numerical simulations are consistent with the theory. Additionally, the results have been compared with those for the GRS 1915+105 black hole, and the hair parameters corresponding to the observed frequencies have been determined.

**KEYWORDS:** numerical relativity, rotating black hole, alternative gravities, Bondi-Hoyle-Lyttleton, QPOs

---

## Contents

|          |  |           |
|----------|--|-----------|
| <b>1</b> | <b>Introduction</b>  | <b>1</b>  |
| <b>2</b> | <b>Equations</b>   | <b>3</b>  |
| 2.1      | General Relativistic Hydrodynamic Equations  | 3         |
| 2.2      | Rotating Black Hole Space-Time Metric in Horndeski gravity   | 5         |
| <b>3</b> | <b>Initial and Boundary Conditions</b>   | <b>6</b>  |
| <b>4</b> | <b>Results</b>   | <b>8</b>  |
| 4.1      | Numerical Results  | 10        |
| 4.2      | The case of $a/M = 0.6$  | 10        |
| 4.3      | The case of $a/M = 0.4$  | 14        |
| 4.4      | A special Case: $a/M = 0.4$ and $h/M = -1.2$   | 16        |
| 4.5      | The case of $a/M = 0.9$  | 16        |
| 4.6      | The case of $a/M = 0.9$ with $h/M = -0.25$ for Different $V_\infty/c$                                      | 18        |
| 4.7      | The Comparison of $V_\infty/c = 0.4$ from $a/M = 0.9$ with $h/M = -0.25$ and $a/M = 0.6$ with $h/M = -0.8$ | 22        |
| <b>5</b> | <b>Possible QPO Models and Observed Frequencies from Numerical Simulations</b>                             | <b>23</b> |
| <b>6</b> | <b>Possible Physical Mechanism and QPOs in M87*</b>  | <b>28</b> |
| <b>7</b> | <b>Understanding the Horndeski parameter-Mass-QPO Relation in GRS 1915 + 105</b>                           | <b>31</b> |
| <b>8</b> | <b>Discussion and Conclusion</b>   | <b>31</b> |

---

## 1 Introduction

Due to various physical reasons, mass accretion in Active Galactic Nuclei (AGNs) and X-ray binary systems causes intense emission of electromagnetic radiation across a wide range of frequencies due to their interactions with the stellar and massive black holes they harbor at their centers. The observation of X-rays emitted as a result of interactions between accreted matter and massive, as well as stellar-mass black holes has yielded significant scientific insights. One of the most notable observational achievements in recent times is the unveiling of the shadows of black holes at the centers of the the *M87* [1, 2] and Milky Way galaxies [3, 4]. Conversely, the observation of Quasi-Periodic Oscillation (QPO) frequencies in X-ray binaries [5–11] over decades is crucial for unveiling the mysteries of the universe and understanding the physical properties of black holes. These observations have illuminated various astronomical phenomena while facilitating the calculation of physical properties such as mass and rotation parameters of the black holes across different

ranges. Therefore, understanding the accretion disks formed by the falling matter toward the black holes and the resulting physical mechanisms is important in gravitational wave astronomy.

There are various models related to mass accretion around compact objects, with one of the most significant being BHL accretion. Initially defined by Bondi and Hoyle and further developed by Lyttleton [12, 13], this phenomenon occurs as an object moves through a medium, forming a disk where matter is gravitationally pulled toward the other side of the compact object. Numerous numerical results on BHL accretion onto black holes exist in the literature, revealing its potential to form accretion disks, shock cones, increase black hole mass through continuous matter accretion, form binary star systems, and produce stars in the interstellar medium. The historical development of BHL accretion and its formulations in both Newtonian and relativistic frameworks can be found in Refs.[14, 15]. Relativistic simulations play a crucial role in revealing the physical properties of the black holes and in explaining  $X$ -ray data observed by detectors, particularly in regions very close to the black hole horizon where gravitational forces are dominant. These simulations yield accurate numerical solutions in areas where gravitational effects are significant, making them essential for understanding phenomena occurring near the black holes. In regions of very strong gravitational forces, numerous simulations related to the Schwarzschild and the Kerr black holes have been conducted to understand the BHL mechanism and contribute to observational results. These simulations are critical for interpreting the complex dynamics near the black holes, where the gravitational effects significantly influence the behavior of the accreting matter [16–25]. In recent years, using alternative theories of gravity, the dynamic structure of the shock cone in regions with very strong gravitational forces has been examined [26–28]. It has been revealed how the shock cone changes depending on various parameters. Simultaneously, the QPO frequencies generated in such systems have been numerically calculated, and their compatibility with observations has been investigated.

Modified gravity has recently gained popularity in numerical relativity due to the limitations of well-known black hole models, such as the Kerr solution, in explaining certain observational results and phenomena like dark matter and dark energy. Alternative theories offer potential solutions to these issues. Alternative theories offer potential solutions to these issues. One such alternative theory is Horndeski, which allows for the coupling of the scalar field with spacetime by defining a 4-dimensional spacetime matrix and is free of Ostrogradski instability [29]. Consequently, the Horndeski black hole is characterized by the scalar hair parameter that describes the scalar field. Both non-rotating and rotating Horndeski black holes have been theoretically studied in the literature, yielding significant progress in solving known astrophysical problems and explaining observational results. These efforts include providing solutions to phenomena such as strong gravitational lensing [30], cosmological studies [31], observed black hole shadows in M87 and the Milky Way galaxy [32], QPO behaviors [33], detection of the photon ring [34–36], the impact of tilted accretion disks on observations [37], and luminosity in thin disks [38].

Studying the accretion disks around the massive black holes by incorporating the effects of scalar fields may help reveal interactions between baryonic matter and dark matter. Because the scalar field is considered one of the candidates that might define dark matter, revealing the impact of the scalar field on the disk formed around the black hole may allow some predictions to be made about the nature of dark matter [25, 39–41]. Similar to Horndeski gravity, the interaction of scalar fields with gravity, through the hair parameter, could play a significant role at both galactic [42] and

cosmic scales [43] in understanding the physical properties of the black holes, and unveiling the mystery of dark matter. Horndeski gravity encompasses a rich content and exhibits parallelism with the observational results in cases of the accelerating expansion of the universe and modifications of gravitational interactions. The scalar hair parameter in Horndeski gravity affects the disk structure near the black hole horizon, the mass accretion process, the emission of gravitational waves, and the shadow of the black hole observed by the Event Horizon Telescope [32, 35].

In this paper, for the first time, we reveal the dynamic structure of the accretion disk and shock cone around the rotating Horndeski black hole in case of the BHL accretion by numerically solving the General Relativistic Hydrodynamic (GRH) equations. To achieve this, we direct matter towards the rotating black hole from the upstream region of the computational domain and examine the effect of the Horndeski gravity scalar field parameter  $h/M$ , namely the scalar hair parameter, on the shock cone, particularly in the strong gravitational fields very close the black hole horizon. We uncover the impact of the hair, asymptotic velocity of the matter injected from outer boundary, and the black hole rotation parameters on the structure of the shock cone, the mass accretion rate, and the produced QPO frequencies inside the shock cone. We compare the numerical solutions computed from the Horndeski black hole with the Kerr solution and attempt to explain some of the observational data.

The organization of the paper is as follows. Section 2 provides the GRH equations and the rotating Horndeski black hole metric. In Section 3, the initial conditions, the range of the hair parameter that is used in numerical simulations, and the boundary conditions are explained. The formation mechanisms of the shock cone at different rotation parameters and scalar field parameter values, how the cone disappears in some extreme cases, and the significant changes in the dynamic structure of the shock cone due to the asymptotic speed with the strong scalar field parameter are described in Section 4. Section 5 numerically reveals the possible QPO frequencies for all models through the power spectrum density analysis, providing detailed information on how QPOs are excited or disappear under different dynamic conditions of the shock cone. The compatibility of the obtained models of the shock cone structures and QPO situations with theoretical studies related to the  $M87^*$  black hole using the possible hair parameters is presented in Section 6. In Section 7, observational results obtained from the GRS 1915 + 105 source are compared with our numerical results, and some QPO and mass limitations are made. Finally, the findings are summarized in Section 8. Throughout the paper, the geometrized units are used, meaning  $G = c = 1$ . Therefore, length and time quantities are expressed in terms of the mass of the black hole.

## 2 Equations

### 2.1 General Relativistic Hydrodynamic Equations

To reveal the physical characteristics of the disk around the black holes and understand the observed data in the strong gravitational region, the General Relativistic Hydrodynamic (GRH) equations are written in conservation form using the 3+1 formalism[44, 45]. Ignoring the effects of magnetic fields and viscosity, the GRH equations on the equatorial plane for a perfect fluid stress-energy tensor are,

$$\frac{\partial U}{\partial t} + \frac{\partial F^r}{\partial r} + \frac{\partial F^\phi}{\partial \phi} = S, \quad (2.1)$$

where  $U$ ,  $F^r$ ,  $F^\phi$ , and  $S$  are conserved variables, fluxes in the  $r$  and  $\phi$  directions, and the source, respectively. The conserved variables, fluxes and sources are written in terms of primitive variables, 3-metric, and other variables defined later as follows.

$$U = \begin{pmatrix} D \\ S_j \\ \tau \end{pmatrix} = \begin{pmatrix} \sqrt{\gamma} W \rho \\ \sqrt{\gamma} \xi \rho W^2 v_j \\ \sqrt{\gamma} (\xi \rho W^2 - P - W \rho) \end{pmatrix}, \quad (2.2)$$

and fluxes are

$$\vec{F}^i = \begin{pmatrix} \alpha \left( v^i - \frac{1}{\alpha \beta^i} \right) D \\ \alpha \left( \left( v^i - \frac{1}{\alpha \beta^i} \right) S_j + \sqrt{\gamma} P \delta_j^i \right) \\ \alpha \left( \left( v^i - \frac{1}{\alpha \beta^i} \right) \tau + \sqrt{\gamma} P v^i \right) \end{pmatrix}, \quad (2.3)$$

and

$$\vec{S} = \begin{pmatrix} 0 \\ \alpha \sqrt{\gamma} T^{ab} g_{bc} \Gamma_{aj}^c \\ \alpha \sqrt{\gamma} (T^{a0} \partial_a \alpha - \alpha T^{ab} \Gamma_{ab}^0) \end{pmatrix}, \quad (2.4)$$

where  $\xi = 1 + \epsilon + P/\rho$  is the enthalpy,  $\Gamma_{ab}^c$  represents the Christoffel symbol,  $W = (1 - \gamma_{i,j} v^i v^j)^{1/2}$  is the Lorentz factor,  $v^i = u^i/W + \beta^i$  donates the three-velocity of the fluid.  $\xi$ ,  $\rho$ ,  $\epsilon$ ,  $\gamma_{i,j}$ ,  $g^{ab}$ ,  $\gamma$ ,  $u^a$ ,  $p$ ,  $\alpha$ , and  $\beta^i$  are the specific enthalpy, the rest-mass density, the internal energy, 3-metric, the four-metric of the curved space-time, the determinant of three-metric, 4- velocity of the fluid, and the fluid pressure, the lapse function, and shift vector, respectively. While the indices  $i, j$ , and  $k$  go from 1 to 3,  $a, b$ , and  $c$  range from 0 to 3.

In this paper, Equation 2.1 is solved numerically to reveal the dynamic structure of the shock cone generated by matter falling towards the black hole in a strong gravitational field. To achieve this, initial values consistent with BHL accretion are defined for the primitive variables. Using these initial values, fluxes are first calculated in the equatorial plane. These fluxes are then used in Riemann solvers to numerically determine the relativistic conservative variables at the next time step. Subsequently, primitive variables are calculated from the computed conservative variables [16, 45, 46]. At this point, the flow speed of the matter must not exceed the speed of light. This situation is known as the "superluminalities" problem. To avoid superluminalities, the following measures are applied in numerical simulations. The Courant condition is used to prevent matter from moving faster than the speed of light within each grid cell. If the matter reaches a speed that could exceed the speed of light, the Courant condition reduces the time step to prevent this situation [45, 46]. Thus, for each model, the time intervals used over approximately 4 million

time steps in numerical simulations are controlled by the Courant condition. Additionally, high-resolution shock-capturing methods and Riemann solvers are used in numerical solutions [15, 47]. These methods specifically prevent superluminal conditions that could occur in shock waves within strong gravitational fields. Moreover, the boundary conditions used also ensure that the speed of the matter remains below the speed of light.

## 2.2 Rotating Black Hole Space-Time Metric in Horndeski gravity

By solving the GRH equations numerically, we reveal the physical structure of the disk around a hairy black hole and its QPO behaviors. For this purpose, in this section, we define the stationary spacetime metric, lapse function, and shift vector of the Horndeski black hole.

As a result of a more detailed examination of Horndeski gravity [29], it was shown that shift-symmetric Horndeski and beyond Horndeski theories can give rise to static and asymptotically flat black holes [48]. However, it was emphasized that the scalar field in this case must have a hair parameter. Theoretical studies concluded that the Lagrangian of Horndeski theory, taking this scalar field into account, is as follows [48].

$$S = \int \sqrt{-g} (Q_2(\chi) + Q_3(\chi)\square\phi + Q_4(\chi)R + Q_{4,\chi} [(\square\phi)^2 - (\nabla^\mu\nabla^\nu\phi)(\nabla_\mu\nabla_\nu\phi)] + Q_5(\chi)G_{\mu\nu}\nabla^\mu\nabla^\nu\phi - \frac{1}{6}Q_{5,\chi} [(\square\phi)^3 - 3(\square\phi)(\nabla^\mu\nabla^\nu\phi)(\nabla_\mu\nabla_\nu\phi) + 2(\nabla_\mu\nabla_\nu\phi)(\nabla^\nu\nabla^\gamma\phi)(\nabla_\gamma\nabla^\mu\phi)]) d^4x, \quad (2.5)$$

where  $\chi = -\partial^\mu\phi\partial_\mu\phi/2$  is canonical kinetic term and  $Q_2, Q_3, Q_4, Q_5$  are arbitrary functions for scalar field  $\phi$ .  $Q_{4,\chi}$  stands for  $\partial Q_4(\chi)/\partial\chi$ ,  $G_{\mu\nu}$  is the Einstein tensor,  $R$  is the Ricci scalar,  $(\nabla_\mu\nabla_\nu\phi)^2 = \nabla_\mu\nabla_\nu\phi\nabla^\nu\nabla^\mu\phi$ , and  $(\nabla_\mu\nabla_\nu\phi)^3 = \nabla_\mu\nabla_\nu\phi\nabla^\nu\nabla^\rho\phi\nabla_\rho\nabla^\mu\phi$ . Using the restriction of scalar field as  $\phi = \phi(r)$  in order to satisfy the static and spherically symmetric spacetime and other restriction given in Ref.[30, 48–50], Horndeski gravity is defined in terms of the determinant of the four-metric, the Ricci scalar, and the scalar field. By imposing the canonical operation of the scalar field and a finite energy condition, solving the field equations results in a static spacetime solution with spherical symmetry for Horndeski gravity [38, 49].

$$ds^2 = -f(r)dt^2 + \frac{dr^2}{f(r)} + r^2(d\theta^2 + \sin^2\theta d\phi^2), \quad (2.6)$$

where  $f(r) = 1 - \frac{2M}{r} + \frac{h}{r}\ln\left(\frac{2}{2M}\right)$ . Here,  $M$  is the mass of the black hole and  $h$  is the scalar hair parameter with the dimension of the length. Horndeski gravity defines the most general scalar-tensor theory with second-order field equations. The hair parameter  $h/M$  can be used to explain different physical results in astrophysical observations by adding the scalar field to the matrix.

For the numerical solution of the GRH equations, it is necessary to define the rotating Horndeski black hole and the surrounding spacetime in Boyer-Lindquist coordinates. To achieve this, the Newman-Janis algorithm is used in Eq.2.6 [50, 51]. Thus, the metric of the rotating hairy black hole is given below [50].

$$ds^2 = - \left( \frac{\Delta - a^2 \text{Sin}^2\theta}{\Sigma} \right) dt^2 + \frac{\Sigma}{\Delta} dr^2 + \Sigma d\theta^2 + \frac{2a \text{Sin}^2\theta}{\Sigma} (\Delta - (r^2 + a^2)) dt d\phi + \frac{\text{Sin}^2\theta}{\Sigma} \left[ (r^2 + a^2)^2 - \Delta a^2 \text{Sin}^2\theta \right] d\phi^2, \quad (2.7)$$

where  $\Delta = r^2 + a^2 - 2Mr + h r \ln\left(\frac{r}{2M}\right)$  and  $\Sigma = r^2 + a^2 \text{Cos}^2\theta$ . Here, the values of  $h/M$  can have an interval  $-2 \leq h/M \leq 0$ . The metric can characterize the rotating black holes for certain values of  $h/M$  and  $a/M$  discussed in Fig.1. The space time around the rotating black hole exhibits a complex dynamics. When the  $h/M \rightarrow 0$ , the Horndeski metric given in Eq.2.7 goes to the Kerr black hole solution [52]. Furthermore, when only  $a/M$  is reduced to zero, it produces a spherically symmetric hairy black hole solution. In addition, the metric transitions to the Schwarzschild solution when both  $h/M$  and  $a/M$  are simultaneously set to zero.

In order to solve the GRH equations with Horndeski space time metric, the lapse function and the shift vectors should be determined in the metric framework. The relationship between the four-metric  $g_{ab}$  and the three-metric  $\gamma_{ij}$ , together with the lapse function  $\alpha$  and shift vectors  $\beta_i$ , is determined using the following relation[53]:

$$\begin{pmatrix} g_{tt} & g_{ti} \\ g_{it} & \gamma_{ij} \end{pmatrix} = \begin{pmatrix} (\beta_k \beta^k - \alpha^2) & \beta_k \\ \beta_i & \gamma_{ij} \end{pmatrix}, \quad (2.8)$$

where the lapse function for Horndeski black hole is

$$\alpha = \sqrt{-\frac{a^2 - \Delta}{\Sigma} + \frac{a^2 (-a^2 + \Delta - r^2)^2}{\Sigma^3}}. \quad (2.9)$$

The shift vectors can be represented as

$$\beta_r = 0, \quad \beta_\theta = 0, \quad \beta_\phi = \frac{a (-a^2 + \Delta - r^2)}{\Sigma}. \quad (2.10)$$

### 3 Initial and Boundary Conditions

BHL accretion occurs when gas falls from the upstream region towards the black hole through the spherical accretion. As a result, it not only creates an accretion disk around the black hole but also leads to the formation of physical mechanisms such as shock waves and cones. These mechanisms can be utilized to comprehend the physical processes underlying the observed QPOs. To identify the type of physical mechanisms formed as a result of BHL accretion, we numerically solve the GRH equations, which describe the behavior of gas within the fixed spacetime around the black hole. In this article, the physical behavior of the shock cone formed around the rotating Horndeski black hole is examined using the Horndeski spacetime matrix. The Horndeski black hole reveals the effects of both the rotation of the black hole and the hair parameters on the formed shock

cone. Thus, our aim is to provide explanations for the physical mechanisms of the observed QPO frequencies, which differ from our previous studies [19, 27, 28, 54, 55].

When modeling the shock cone around the Horndeski black hole, the matter is sent from the upstream region with spherical accretion from the outer boundary of the computational domain. The physical properties of the sent matter include:  $\rho = 1$ ,  $C_\infty = 0.1$ ,  $\Gamma = 4/3$ ,  $V^r = \sqrt{\gamma^{rr}}V_\infty \cos(\phi)$ ,  $V^\phi = -\sqrt{\gamma^{\phi\phi}}V_\infty \sin(\phi)$  are the rest-mass density, the sound speed, the adiabatic index of the matter, radial velocity, and angular velocity of the injected matter, respectively. The pressure of the falling matter is computed using the ideal gas equation of state,  $P = (\Gamma - 1)\rho\epsilon$ . In most models, we use the asymptotic speed of  $V_\infty/c = 0.2$ . However, to reveal the impact of the asymptotic speed on the shock cone and to make comparisons with the literature, we also employ the different asymptotic speeds, as shown in Table 1. During the formation of the shock cone in BHL accretion,  $V_\infty/c$  plays a significant role in creating an effect. This effect has been extensively discussed in the literature across the different gravities [16, 18, 19, 22–26, 56–58]. However, in our upcoming article, we will extensively discuss the impact of  $V_\infty/c$ , considering the scalar hair and the rotation parameter of the black hole as well. At the same time, we will reveal the effect of the adiabatic index ( $\Gamma$ ) on the formation of shock cones. Since gas can be more compressible at higher values of  $\Gamma$ , we will examine the condition for the forming a bow shock in these calculations. The formation of the bow shock is a physical mechanism observed in the case of an ultralight scalar field, under different  $\Gamma$  and  $V_\infty/c$  [25].

In this study, the scalar hair parameter ( $h/M$ ) in Horndeski gravity constitutes the main theme of our work. We will investigate the effect of this parameter on the mass accretion rate and the creation of the shock cone around the rotating black holes. However, not every value of  $h/M$  in Horndeski gravity results in a rotating black hole. There exists a critical value of  $h/M$  for each rotation parameter. Only if  $h/M < h_c/M$  is there a black hole solution. Fig.1 shows the  $h_c/M$  for different rotation parameters.  $h_c$  are determined from the analytic calculation using the spacetime metric of Horndeski. For every  $h/M$  value that lies below the curve shown in Fig.1, the black hole is formed. The  $h/M$  values given in Table 1 have been selected according to this situation.

The computational domain used to construct a stable shock cone around the Horndeski black hole is  $r \in [2.3M, 100M]$  and  $\phi \in [0, 2\pi]$ . A grid spacing of equal distance in both radial and angular directions are utilized. In the radial direction, 1024 points are used, while in the angular direction, this value is 256. For all models, a maximum time of  $t_{max} = 35000M$  has been set. The reason for running the codes for such a long duration is to examine the behavior of the shock cone after it has reached the steady-state. This is crucial because QPO frequencies are determined based on this behavior.

As seen in Table 1, the shock cone reaches a steady-state around  $t = 2000M$ . Subsequently, it has exhibited instability behavior around the certain value. Drawing from extensive experience with QPOs, we are confident that QPO frequencies do not depend on grid resolution [26–28, 58].

At the outer boundary of the computational domain in radial direction, two different situations are present. Since gas is continuously injected into the computational domain from the upstream region, the same value has been used in the boundaries of the upstream region. However, an outflow boundary condition has been applied to expel the numerical issues at the boundary caused by the gas reaching the downstream region. On the other hand, an outflow boundary condition has been implemented at the inner boundary of the computational domain. This means that the gas



**Table 1.** The initial model adopted for the numerical simulation of Kerr and Horndeski metric and some outcomes produced from the numerical results.  $Model$ ,  $type$ ,  $a/M$ ,  $h/M$ ,  $V_\infty/c$ ,  $r_{stag}/M$ ,  $\theta_{sh}/rad$ , and  $\tau_{ss}$  are the name of the model, the gravity, the black hole rotation parameter, scalar hair parameter in Horndeski metric, asymptotic velocity of gas injected from the outer boundary, the position of the stagnation point, shock cone opening angle, and time to require to reach the steady-state, respectively.

| $Model$         | $type$           | $a/M$ | $h/M$ | $V_\infty/c$ | $r_{stag}/M$ | $\theta_{sh}/rad$ | $\tau_{ss}/M$ |
|-----------------|------------------|-------|-------|--------------|--------------|-------------------|---------------|
| $H04A$          | <i>Kerr</i>      | 0.4   | 0     | 0.2          | 27.2         | 1.076             | 2561          |
| $H04B$          |                  | 0.4   | -0.5  | 0.2          | 14.05        | 0.782             | 7900          |
| $H04C$          | <i>Horndeski</i> | 0.4   | -0.8  | 0.2          | 10.6         | 0.561             | 4600          |
| $H04D$          |                  | 0.4   | -1.0  | 0.2          | 9            | 0.344             | 1900          |
| $H04E$          |                  | 0.4   | -1.2  | 0.2          | 8.3          | <i>NO</i>         | <i>NO</i>     |
| $H06A$          | <i>Kerr</i>      | 0.6   | 0     | 0.2          | 27           | 1.052             | 2400          |
| $H06B$          |                  | 0.6   | -0.1  | 0.2          | 23.3         | 1.028             | 1900          |
| $H06C$          | <i>Horndeski</i> | 0.6   | -0.2  | 0.2          | 20.2         | 0.979             | 1700          |
| $H06D$          |                  | 0.6   | -0.4  | 0.2          | 15.9         | 0.88              | 1400          |
| $H06E$          |                  | 0.6   | -0.6  | 0.2          | 12.5         | 0.708             | 4550          |
| $H06F$          |                  | 0.6   | -0.8  | 0.2          | 10           | 0.537             | 4150          |
| $H06V_\infty04$ |                  | 0.6   | -0.8  | 0.4          | 7.1          | 0.684             | 4000          |
| $H09A$          | <i>Kerr</i>      | 0.9   | 0     | 0.2          | 26.85        | 1.052             | 2350          |
| $H09B$          |                  | 0.9   | -0.1  | 0.2          | 23.3         | 1.027             | 2300          |
| $H09C$          | <i>Horndeski</i> | 0.9   | -0.15 | 0.2          | 21.8         | 1.003             | 2100          |
| $H09D$          |                  | 0.9   | -0.2  | 0.2          | 20.5         | 0.979             | 1900          |
| $H09V_\infty02$ |                  | 0.9   | -0.25 | 0.2          | 19.35        | 0.954             | 1800          |
| $H09E$          |                  | 0.9   | -0.27 | 0.2          | 18.5         | 0.93              | 1700          |
| $H09V_\infty01$ |                  | 0.9   | -0.25 | 0.1          | 27.3         | 1.077             | 2080          |
| $H09V_\infty04$ |                  | 0.9   | -0.25 | 0.4          | 9.4          | 0.806             | 970           |
| $H09V_\infty06$ |                  | 0.9   | -0.25 | 0.6          | 5.8          | 0.757             | 370           |

approaching the horizon is expelled from the computational domain, signifying the matter falling into the black hole. Periodic boundary conditions are enforced in the  $\phi$ -direction to preserve the symmetry of the physical solutions..

## 4 Results

In this section, we model the dynamics of the shock cone numerically and reveal its formation around the rotating Horndeski black hole as a result of BHL accretion. We also attempt to understand the dynamic behavior of the shock cone on the downstream side of the computational domain. We uncover how the dynamic structure of the shock cone and the physical behavior of the trapped and excited QPOs change with the black hole rotation parameter ( $a/M$ ), scalar hair parameter of the Horndeski gravity ( $h/M$ ), and asymptotic velocity of the injected matter injected from the outer boundary in the upstream region ( $V_\infty/c$ ).

BHL accretion occurs when matter falls onto an object moving supersonically through a uniform medium, leading to non-spherical accretion of matter only on one side of the object. On the other side of the object, matter accretion is very weak. This is the fundamental difference that distinguishes BHL accretion from spherical Bondi accretion. Numerical calculations conducted

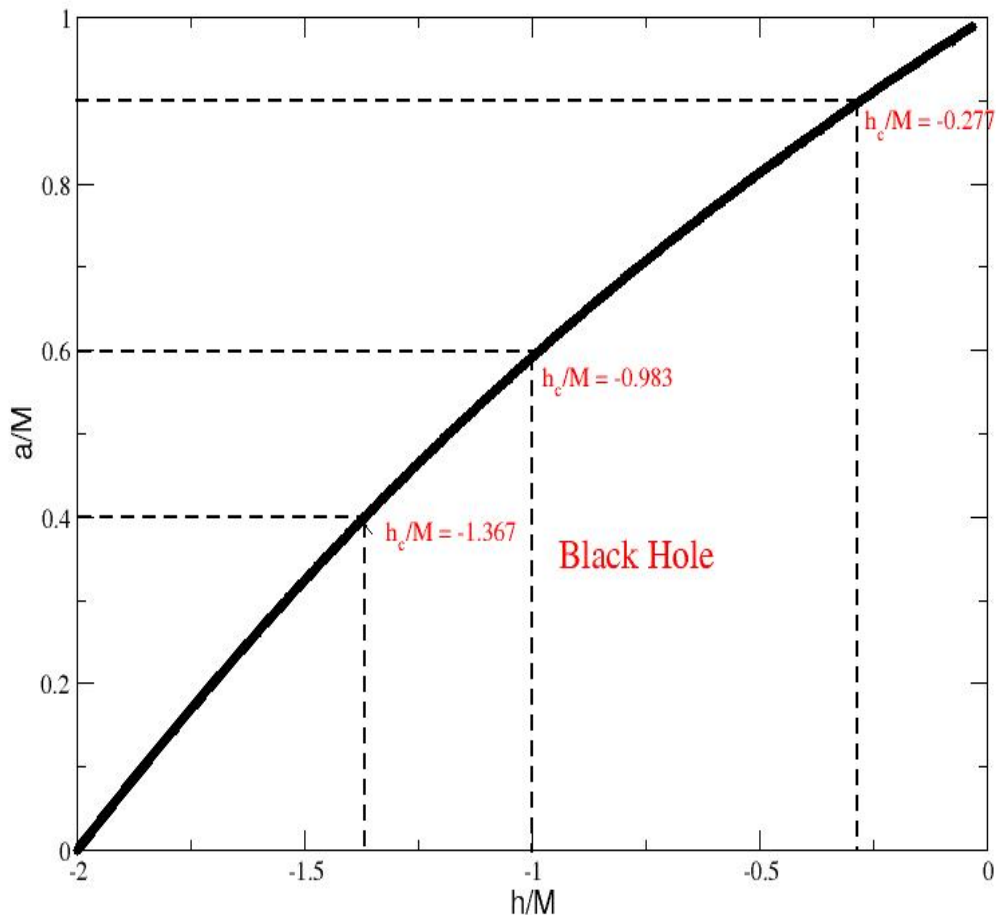


**Figure 1.** The critical values of the scalar hair parameter ( $h/M$ ) that the Horndeski matrix depends on, according to the black hole rotation parameter ( $a/M$ ). There exists a maximum possible value for  $h/M$  for every given value of  $a/M$ . Black hole solutions exist for values of  $a/M$  and  $h/M$  that have been located under the curve shown in the figure. The values in Table 1 are selected according to this plot.

over many years have shown that BHL accretion results in the formation of a shock cone on the opposite side of the object [14, 19, 22, 23, 57]. This cone itself demonstrates that the accretion is non-spherical [16, 24]. If the object is a black hole, the shock cone formed by this accretion can extend to the inner boundary of the computational domain, i.e., close to the black hole’s horizon, making the shock cone an important physical mechanism for revealing the frame-dragging effect in strong gravitational fields. Additionally, the oscillation modes trapped within the cone are an important physical mechanism for producing QPO frequencies. Our current studies and existing literature show that BHL accretion is a significant mechanism because of these features. Shock cones that can form very close to the black hole’s horizon in strong gravitational fields emerge as an important mechanism for explaining many observational data [16, 18, 25, 59]. Furthermore, as demonstrated in this study, it is also an important mechanism for revealing the effect of scalar fields [60] and for testing alternative gravities [26, 28, 58] on the physical mechanisms around the black

hole. Thus, the differences between modified gravities and Kerr gravity can be understood through the BHL accretion mechanism.

#### 4.1 Numerical Results

Understanding the behavior of the stagnation point around the black hole helps determine the accretion speed of the matter falling towards the black hole and thus aids in understanding the spectral energy distribution. Fig.2 shows the behavior of the stagnation point for different black hole spin parameters according to the scalar hair parameter. As seen in the figure, while the behavior of the stagnation point undergoes significant changes with the variation of the hair parameter, this change is not obvious in the case of different spin parameters. As the hair parameter increases in the negative direction, as seen in Fig.2, the stagnation point approaches the black hole horizon with an exponential decrease. This change, as discussed in more detail later, leads to the sweeping outwards of the shock cone, thereby causing a change or complete disappearance of the QPO frequencies.

On the other hand, as seen in Table 1, an increase in the asymptotic speed also causes the stagnation point to approach the black hole horizon. However, the behavior of the shock cone in this case is completely different from that in the case of the hair parameter. In this scenario, more matter is accumulated within the shock cone, especially close to the event horizon leading to a change and then disappearance of the QPO frequencies.

The variation in the maximum value of the mass accretion rate after the shock cone has reached a steady-state is presented as a function of  $h/M$  in Fig.3. In the numerical calculations, the mass accretion is computed close to the black hole horizon, specifically at  $r/M = 4M$ . Subsequently, the changes with the scalar hair and the black hole rotation parameter are depicted in Fig.3. Again, the impact of the rotation parameter on the mass accretion rate has not been observed in a pronounced manner. However, the scalar hair parameter has significantly reduced the mass accretion rate. Figs.2 and 3 show a complete correlation between the behaviors of the stagnation point and the mass accretion rate, which is an expected outcome. The most fundamental difference between them is that the stagnation point creates an inwardly curved line, while the mass accretion rate forms an outwardly curved line.

Understanding the mass accretion rate around the black holes significantly contributes to explaining many astrophysical phenomena. For instance, a high mass accretion rate leads to matter falling into the black hole and, as a result, causes electromagnetic emissions in the strong gravitational field. Additionally, as matter falls into the black hole regularly, it increases the mass of the black hole. Thus, this can explain the existence of massive black holes.

#### 4.2 The case of $a/M = 0.6$

The morphology is shown in Fig.4 long after the shock cone has reached the steady-state ( $t \sim 2000M$ ), and at a much later time ( $t = 32000M$ ). The figure illustrates the change in the rest-mass density and the formation of the shock cone around the Kerr and Horndeski black holes with a rotation parameter of  $a/M = 0.6$ , using a colormap and isocontours. The top left graph displays the morphology of the rest-mass density in Kerr gravity, while the others showcase the dynamics of the shock cone around the Horndeski black hole under different scalar hair parameters ( $h/M > h_c/M = -0.983$ ).

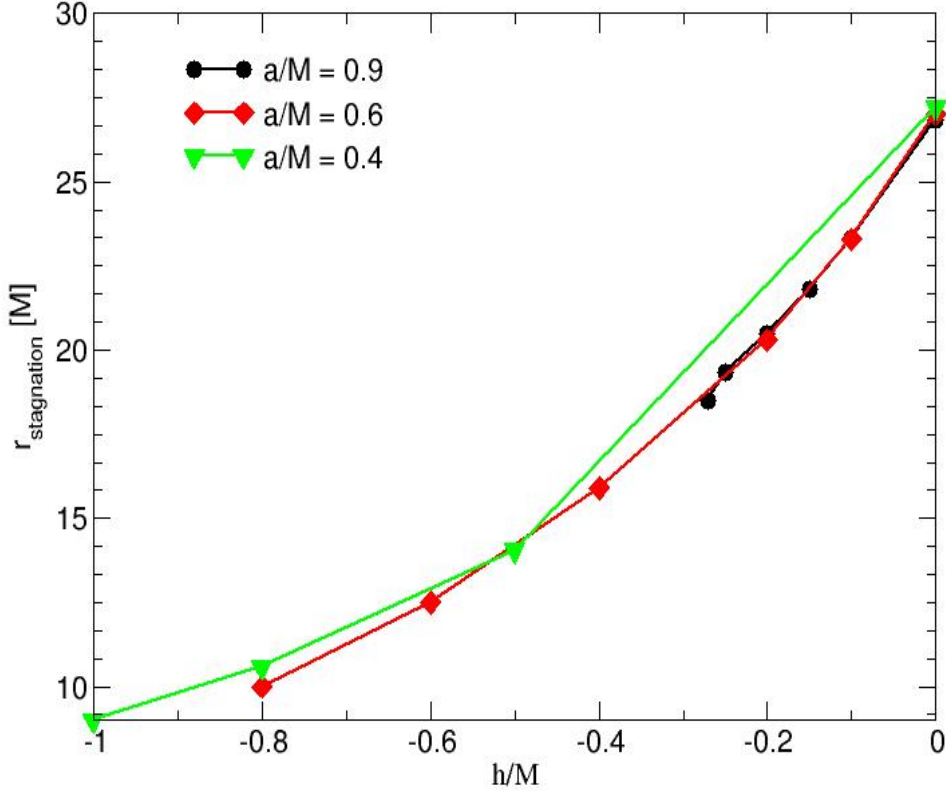


**Figure 2.** The radial position of the stagnation point as a function of Horndeski hair parameter. The changes in the stagnation point under different black hole rotation parameters and possible hair parameters have been demonstrated.

The BHL accretion mechanism has been extensively studied in the literature across various gravitational models, such as Kerr, Einstein-Gauss-Bonnet, and Hartle-Thorne [16, 18, 19, 25? – 27]. It has been observed that the shock cone forms regardless of the gravity model employed. BHL accretion results from the matter falling towards the black hole supersonically from the upstream region, leading to the formation of the shock cone on the downstream side. The shock cone has been observed at various values of  $h/M$  as seen in Fig.4. Although the shock cone forms for every value of  $h/M$ , it has been observed that, unlike with other gravity models, the scalar hair parameter in Horndeski gravity significantly affects the dynamic structure of the shock cone. When considering aspects such as the cone opening angle and the stagnation point, as shown in Table 1, it is evident in Fig.4 that as  $h/M$  increases in the negative direction, the dynamic structure of the shock cone undergoes a significant change.

The interaction of the scalar field with spacetime alters the behavior of matter on the downstream side. As  $h/M$  increases in the negative direction, indicating an intensification of the scalar field, the opening angle of the formed shock cone decreases. Concurrently, the rate at which trapped matter falls into the black hole diminishes with  $h/M$ . In essence, as the force created by the scalar

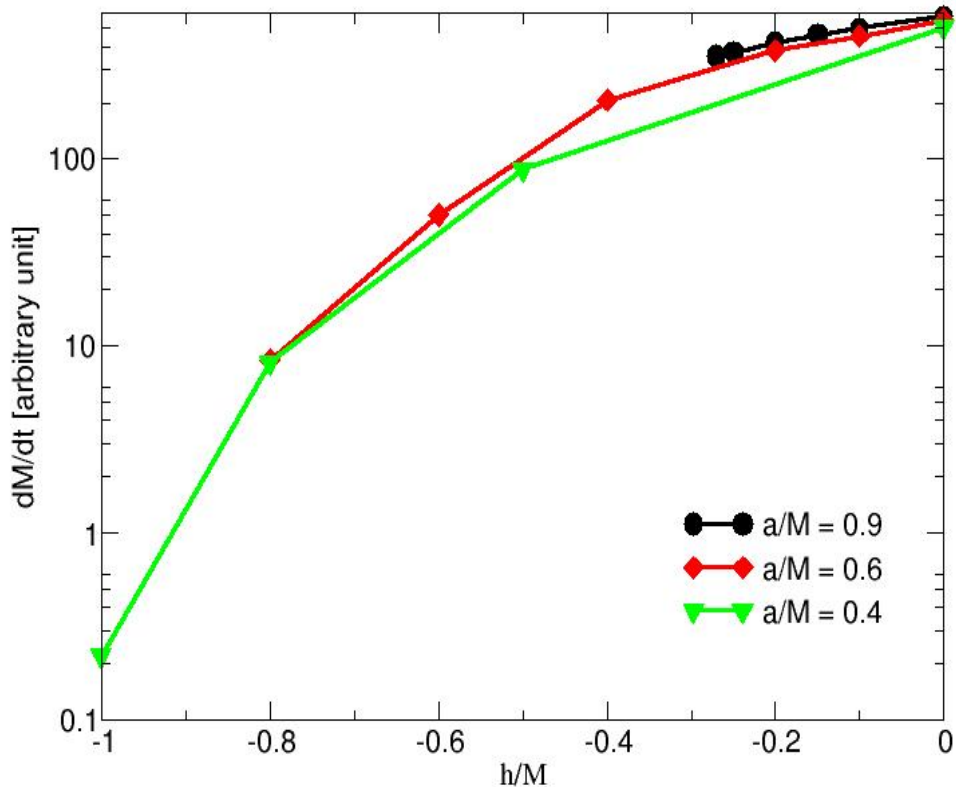


**Figure 3.** The change in the mass accretion rate depending on Horndeski hair parameters for different black hole rotation parameters with  $V_\infty/c = 0.2$ . Each point on the figure has been calculated long after the shock cone reaches to the steady-state at  $r = 4M$ .

field intensifies with  $h/M$  becoming more negative, the matter begins to move further away from the black hole. This shift also causes the stagnation point to move closer to the black hole horizon. These physical changes are clearly observable in the  $h/M = -0.6$  and  $h/M = -0.8$  models. This intriguing result suggests that the shock cone is on a trajectory towards disappearance as  $h/M$  varies. Consequently, the change in the dynamic structure of the shock cone has resulted in alterations to the oscillation frequencies of trapped pressure-based and radial-based QPO modes, and even their disappearance. The possible QPOs are discussed in detail in Section 5.

The variation in the mass accretion rate near the black hole horizon, at  $r = 4M$ , is depicted in Fig.5. It is evident that the shock cone has reached the steady-state in all models. However, the time required to reach this steady-state varies, as indicated in Table 1. The behavior of the mass accretion rate confirms the discussions presented in Fig.4 and the numerical results listed in Table 1. The influence of the scalar hair parameter, which leads to a decrease in the amount of matter falling towards the black hole, is distinctly visible in Fig.5. As  $h/M$  becomes more negative, the stagnation point shifts closer to the black hole, thereby deflecting more matter away from it. Consequently, there is a reduction in the mass accretion rate, implying that the quantity of

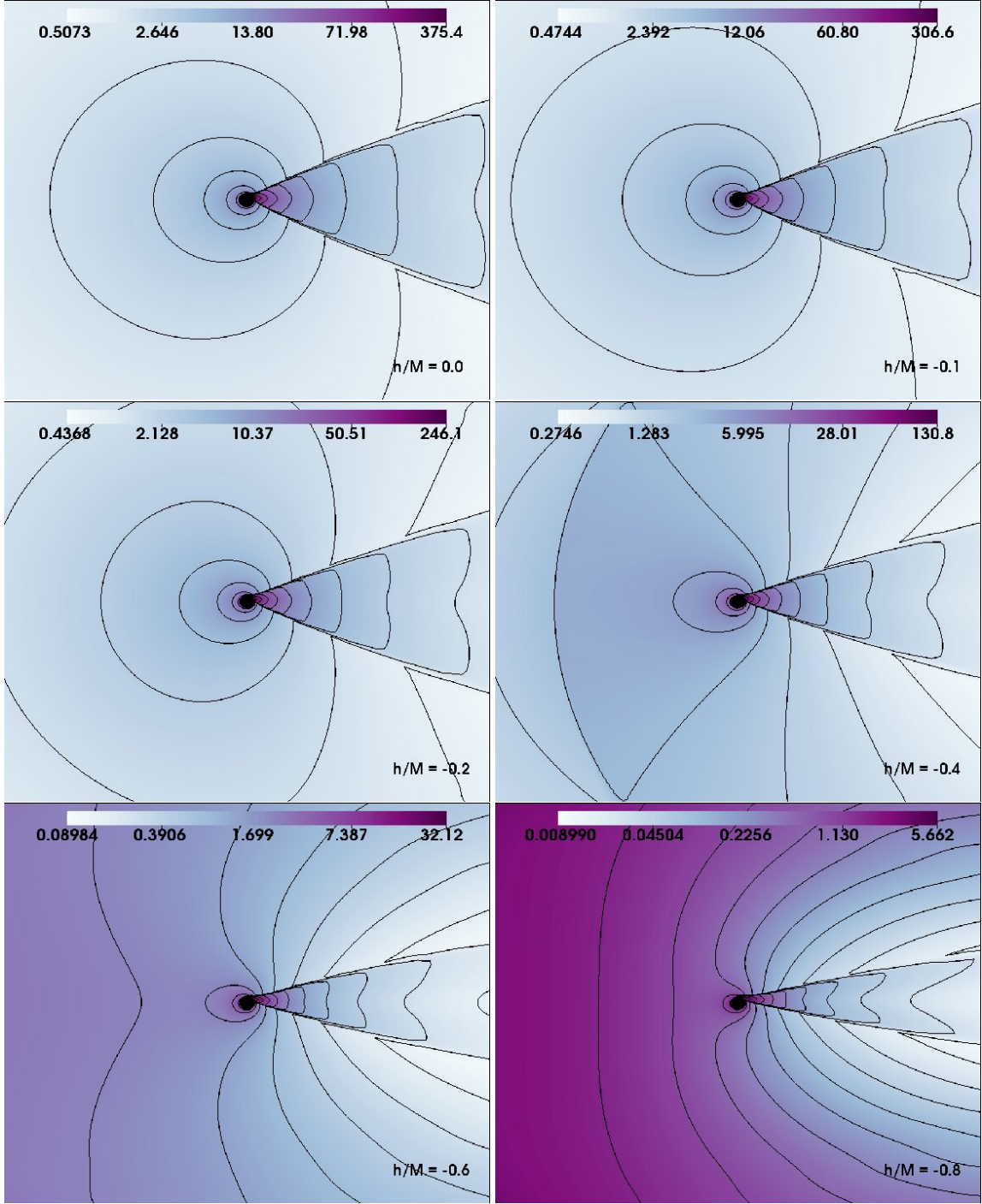


**Figure 4.** The rest-mass density variations across the different Horndeski parameters on the equatorial plane for  $a/M = 0.6$  are shown, using the both color and contour lines at the end of the numerical evolution  $t = 35000M$ . As seen in Table 1, each model has reached the steady-state well before the maximum time. In particular, to observe the dynamic structure of the shock cone close to the black hole in more details, the minimum and maximum limits on the  $x$  and  $y$  axes have been set from  $-70M$  to  $70M$ .

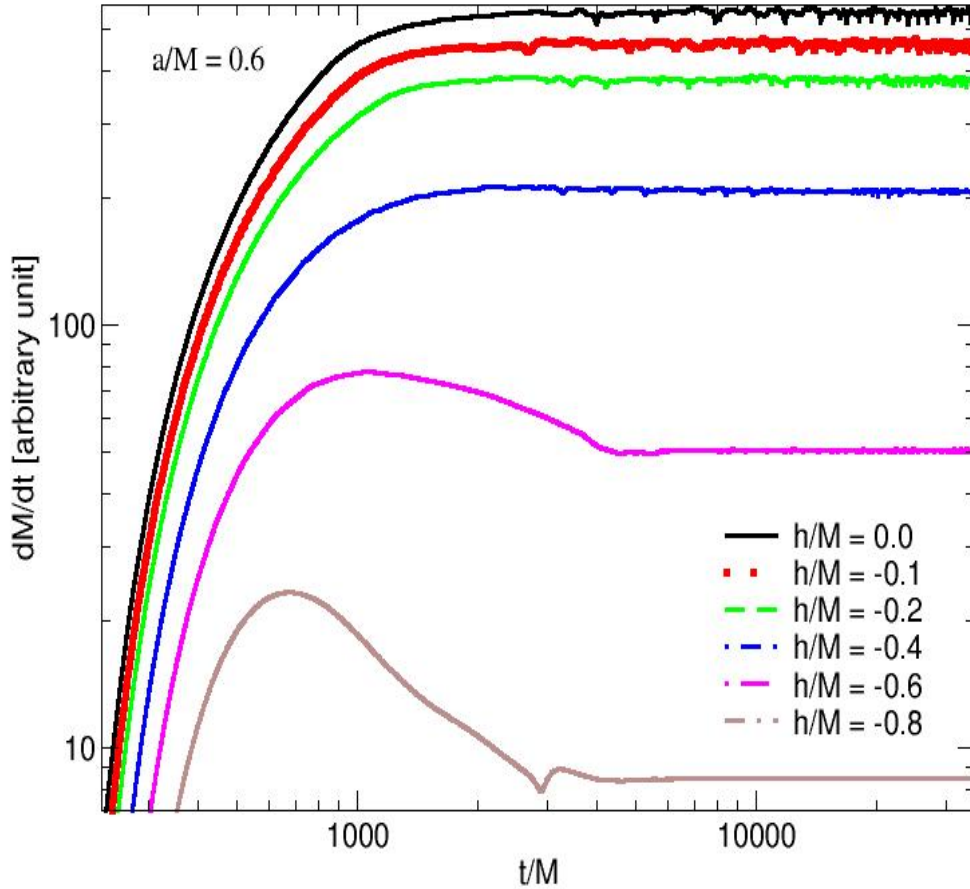


**Figure 5.** The change in mass accretion rate over time for  $a/M = 0.6$ , demonstrated for each Horndeski hair parameter. The effect of the scalar hair parameter on the dynamics of the mass accretion rate around the black hole is shown.

matter being absorbed by the black hole diminishes over time. Notably, as demonstrated in Fig. 5 the dynamic structure of the shock cone at  $h/M = -0.6$  and  $h/M = -0.8$  exhibits significant variances when compared to other values of  $h/M$ . This suggests that the behavior of the shock cone undergoes more rapid changes once the stagnation point descends a certain threshold, which occurs for  $h/M < -0.4$ . Moreover, post-reaching the steady state, the shock cone displays instability, and the mass accretion rate hints at the emergence of QPOs. However, as discussed in Section 5, no QPO frequencies are observed in the model with  $h/M = -0.8$ .

### 4.3 The case of $a/M = 0.4$

To uncover the structure of the shock cone formed around the Horndeski black hole due to the interaction of spacetime with a strong scalar field, we model the scenario with a small rotation parameter. For  $a/M = 0.4$ , Fig. 6 demonstrates how the dynamic structure of the shock cone changes in the presence of both weak and strong scalar fields, while also comparing it to the Kerr

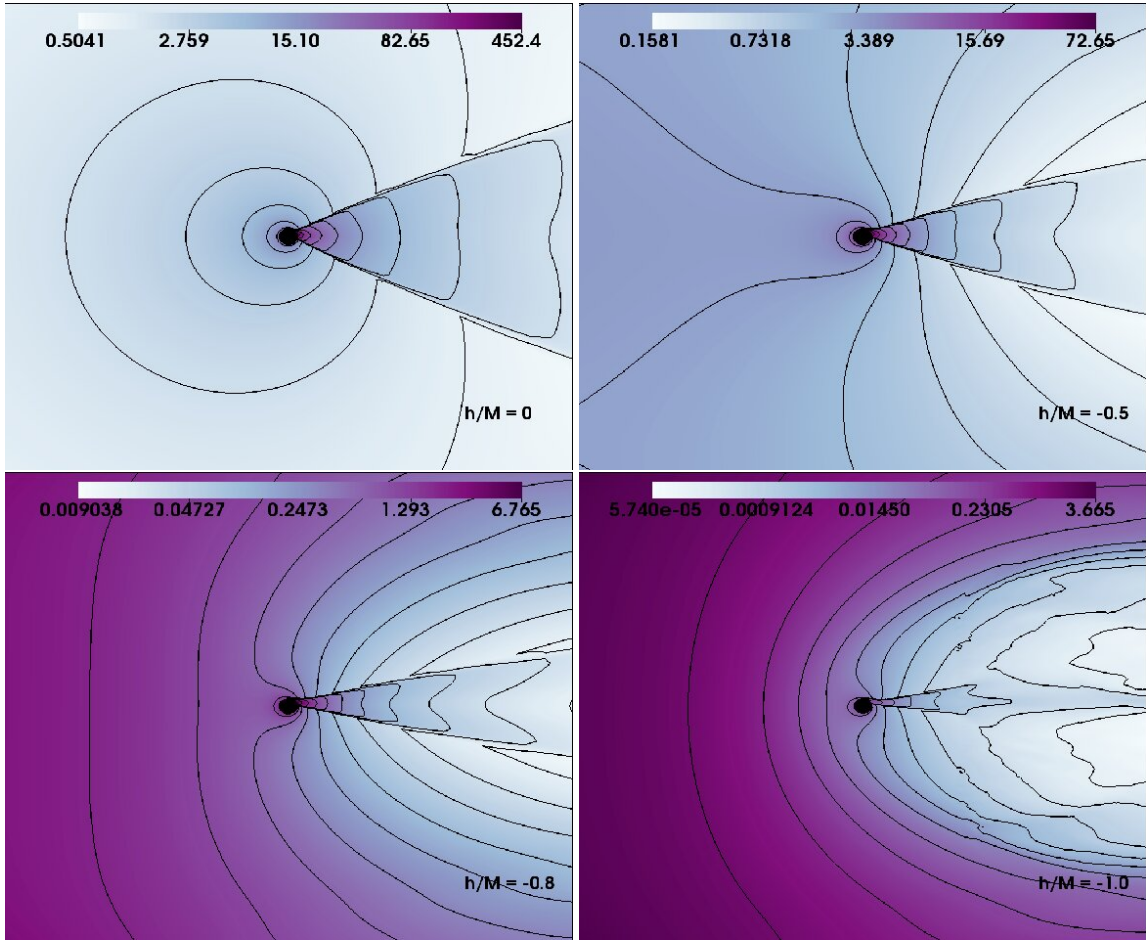


**Figure 6.** Same as in Fig.4 but for the  $a/M = 0.4$ .

solution.

The growth of the scalar field parameter  $h/M$  in the negative direction has significantly altered the structure of the shock cone formed on the downstream side of the computational domain around the black hole. Due to the increased effect of the field as  $h/M$  changes, more matter within the shock cone has been pushed away from the black hole. As a result, the shock cone has entered a process of disappearance. In Section 4.4, the stronger scalar field defined with  $h/M = -1.2$  has been modeled, and it is observed that the cone completely vanishes. Consequently, QPO frequencies, which could have been generated by the pressure and radial modes trapped entirely within the shock cone, do not form. Indeed, our results for the rotation parameters  $a/M = 0.4$  and  $a/M = 0.6$  strongly support the notion that the shock cone is one of the most significant physical mechanisms that can be proposed to explain observational QPOs.



#### 4.4 A special Case: $a/M = 0.4$ and $h/M = -1.2$

The possible analytical values of the scalar hair parameter are presented in Fig.1. As the rotation parameter of the black hole increases,  $h/M$  approaches zero. This implies that models of rapidly rotating black holes have a narrower range of  $h/M$  compared to other rotation cases. For the slowly rotating black hole model, specifically  $a/M = 0.4$  with  $0 \geq h/M > h_c/M = -1.3670$ , it is beneficial to examine the dynamical changes of the shock cone with respect to  $h/M$  during BHL accretion. Therefore, we model the extreme cases of the scalar field with  $h/M = -1.2$ . In Fig.7, the formation of the shock cone at  $h/M = -1.2$  is depicted. This plot illustrates the cone formation over time. However, due to the strong interaction of the scalar field with spacetime, it is observed that all matter reaching the downstream side of the computational domain is pushed towards the outer boundary of the computational region, away from the black hole. Consequently, in the case of  $a/M = 0.4$  with  $h/M = -1.2$ , no shock cone forms, and all matter reaching the downstream region is observed to move away from the black hole. Due to the chaotic behavior of the dynamics, the code crashed after a certain period. Fig.8 again displays the behaviors of different physical parameters for the same model in one dimension. As can be seen, no shock cone has formed, indicating that no mechanism capable of trapping QPO modes has been established.

Sections 6 and 7 have already discussed the possible  $h/M$  values for  $M87^*$  [32] and GRS 1915+105 [61, 62] sources. The observational results obtained from these sources have been compared with theoretical outcomes to define the possible range of  $h/M$ . Considering the possible  $h/M$  values for these sources, it is observed that  $h/M = -1.2$  significantly deviates from the values calculated based on observations. In fact, the calculations demonstrate the accuracy of the numerical model results. Since no shock cone forms at  $h/M = -1.2$ , it is not possible to form QPOs, and consequently, reliable observation in this model is unattainable.

#### 4.5 The case of $a/M = 0.9$

In Fig.9, we model the morphology of the shock cone around a rapidly rotating ( $a/M = 0.9$ ) Horndeski black hole with scalar hair. As observed in Fig.9, given that the critical value of the hair parameter for this rotation parameter is  $h_c/M = -0.27$ , we explore the physical structure of the shock cone at various  $h/M$  values. In this scenario, since the scalar field cannot be as strong as it is for other rotation parameters, the structure of the shock cone is maintained across all models. However, we noted a tendency for the maximum density of the cone to decrease as  $h/M$  becomes more negative. This alteration impacts the formation of pressure and radial modes, leading to changes in the intensity and frequencies of the excited modes. Specifically, the frequencies increase as  $h/M$  decreases. The variation of QPO frequencies for different  $h/M$  values in the case of  $a/M = 0.9$  is discussed in detail in Section 5.

As seen in the case of  $a/M = 0.9$ , the variation in the mass accretion rate for different  $h/M$  values is depicted in Fig.10. As  $h/M$  becomes more negative, indicating an increase in the intensity of the scalar field, more matter is pushed outwards in the region where the shock cone is located, leading to a decrease in the mass accretion rate. This clearly signals a change in the physical structure of the shock cone. Naturally, this change also impacts the QPO frequencies.

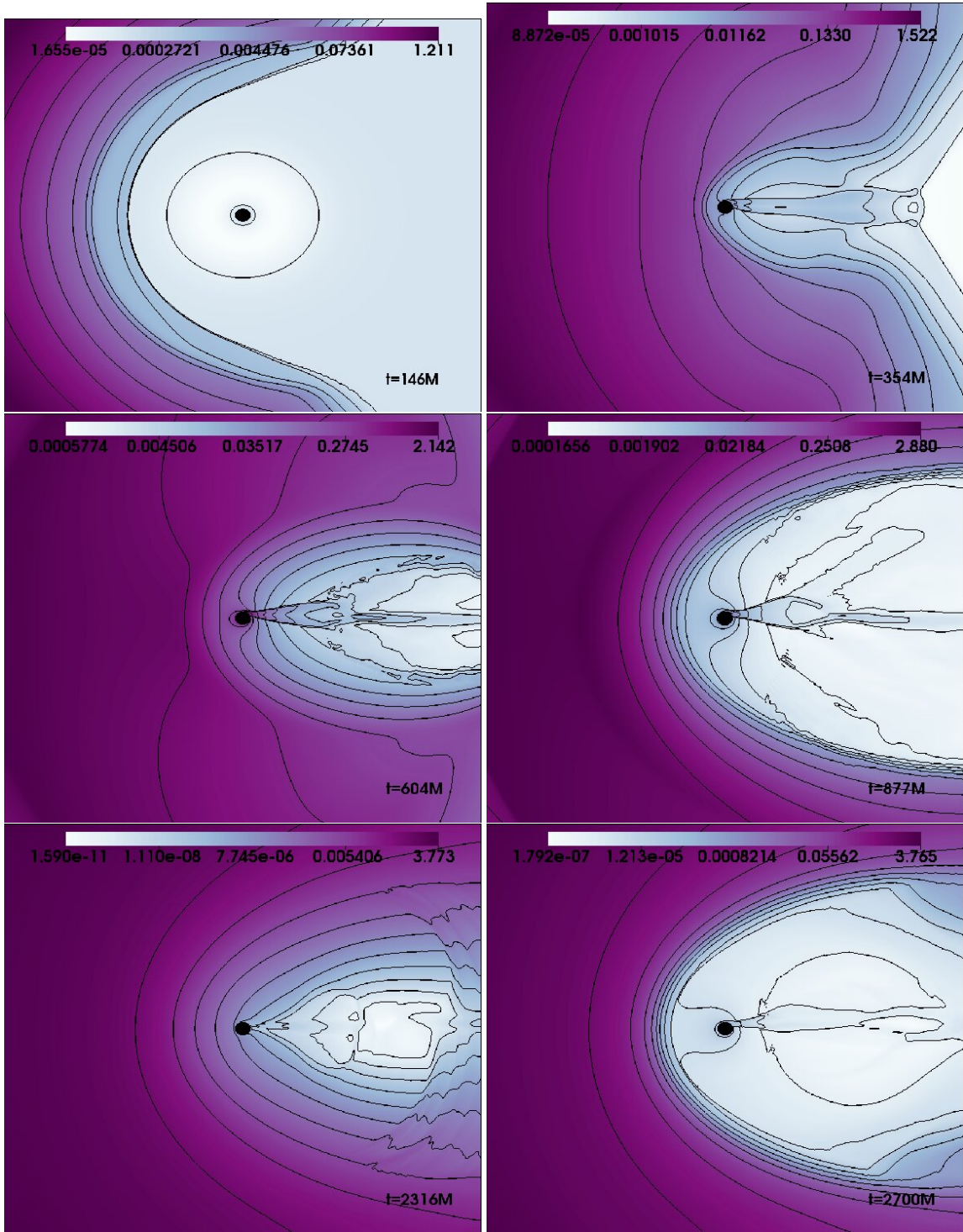


**Figure 7.** The Color and counter maps of the rest-mass density in 2D for  $a/M = 0.4$  with  $h/M = -1.2$ . Each snapshot shows the change in the shock cone dynamic structure at different times of the same model. It demonstrates how the shock cone on the downstream side disappears due to the stagnation point getting closer to the black hole. At the same time, it shows that the conditions in the middle and bottom rows exhibit similar behavior. Namely, in the region where the shock cone is located, an oscillation state encountered, for the first time, has been observed.

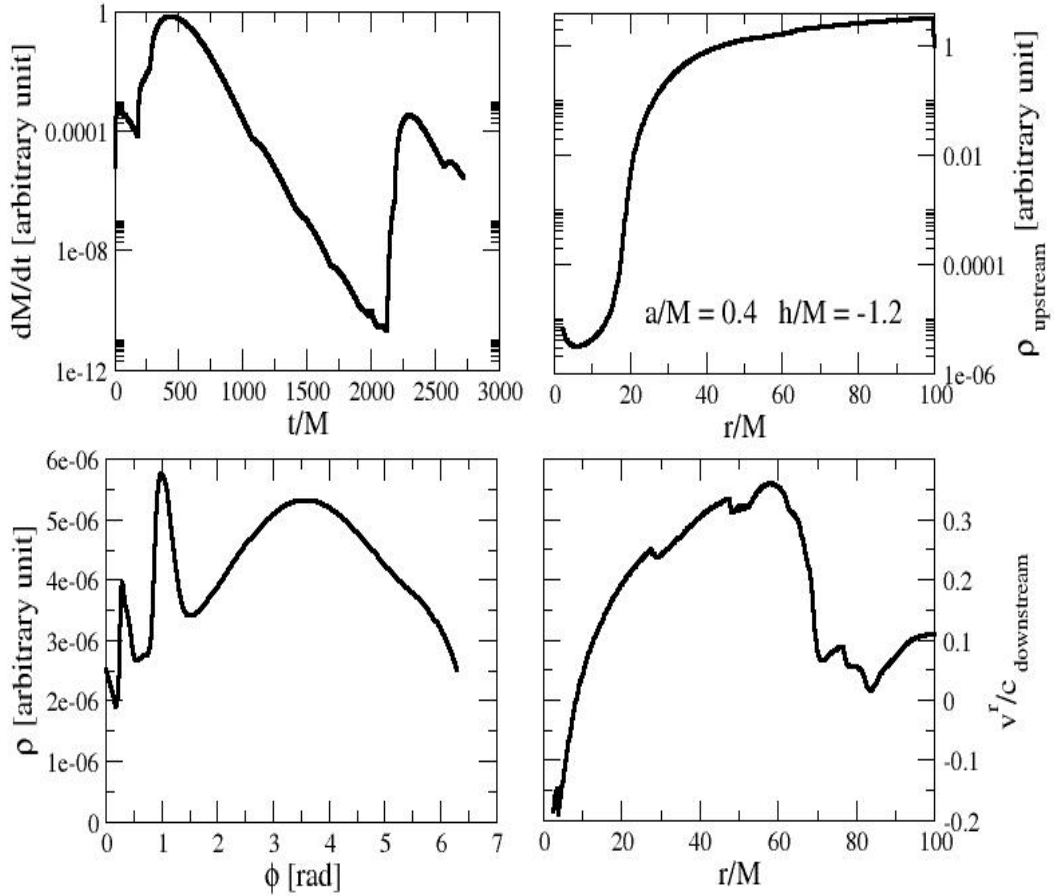


**Figure 8.** The variation of the different values of the shock cone in the vicinity of the Horndeski black hole for the  $a/M = 0.4$  with  $h/M = -1.2$ . Upper left: This section illustrates the changes in the mass accretion rate. Upper right: Here, the rest-mass density on the upstream side of the computational domain is depicted along the radial direction at  $\phi = 3.14$  rad. Lower left: A one-dimensional representation of the rest-mass density is shown along the azimuthal direction, positioned at  $r = 2.68M$ , very near the black hole horizon. Lower right: Displayed is the radial velocity along the radial axis at  $\phi = 0.024$  rad in downstream side.

#### 4.6 The case of $a/M = 0.9$ with $h/M = -0.25$ for Different $V_\infty/c$

It is known from studies on Kerr [18, 22, 23, 56] and EGB [26, 27] gravity models that the asymptotic speed of matter falling into the black hole supersonically during BHL accretion significantly impacts the mass accretion and the physical structure of the shock cone. In this study, for the rapidly spinning black hole model with  $a/M = 0.9$  and a hair parameter close to the critical value of  $h/M = -0.25$ , we demonstrate how the mass accretion (as shown in Fig.12) and the dynamics of the shock cone (as shown in Fig.11) vary depending on the asymptotic speed.

As shown in Fig.11 and Table 1, at the lowest value of the asymptotic speed, both the shock cone opening angle and the time required to reach the steady state are large. However, these values decrease as the asymptotic speed increases. Concurrently, the stagnation point moves closer to

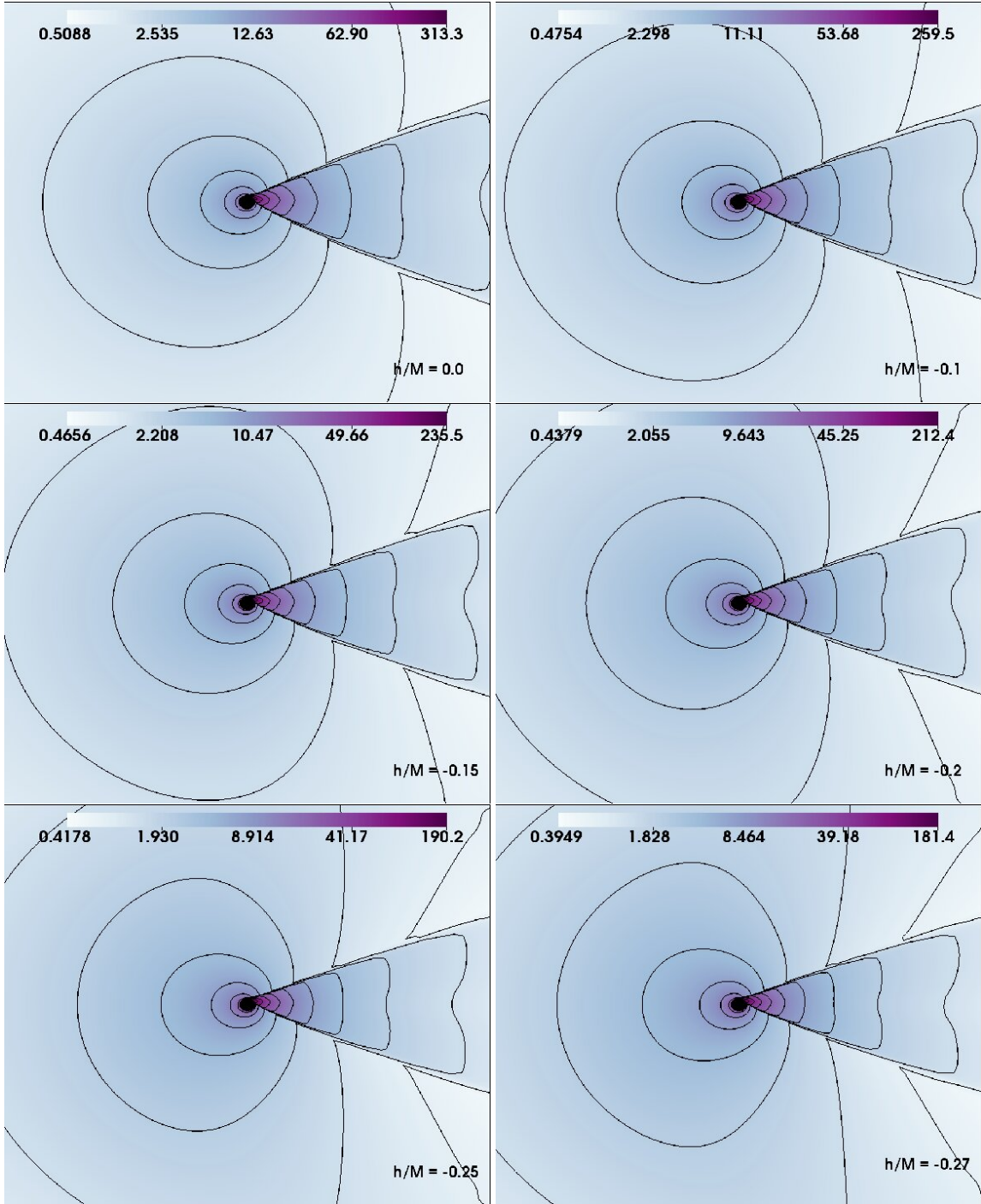


**Figure 9.** Same as in Fig.4 but for the  $a/M = 0.9$ . As seen in Fig.1, due to the limited value of  $h/M \leq -0.277$ , the maximum value of the hair parameter used for the case is  $-0.27$ .

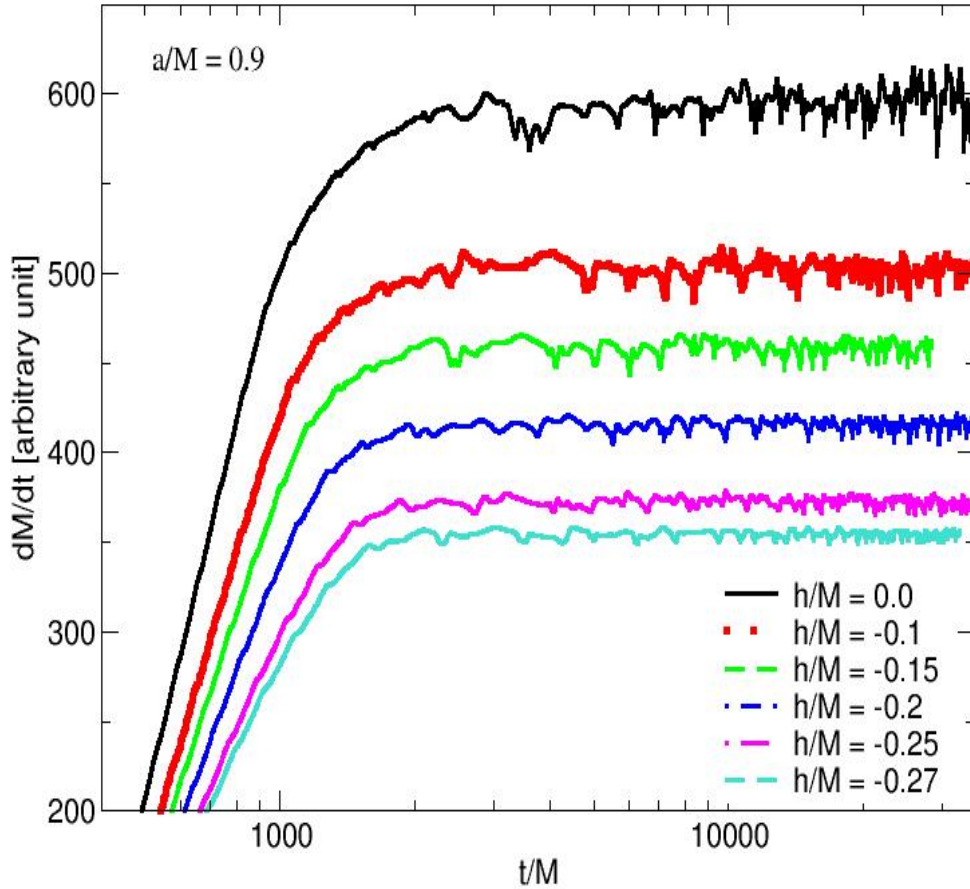


**Figure 10.** Same as in Fig.5 but it is for  $a/M = 0.9$

the black hole horizon, while the rest-mass density of the matter trapped within the shock cone increases. At  $V_\infty/c = 0.1$  and  $V_\infty/c = 0.2$ , the dynamics of the shock cone and the QPO modes excited within it exhibit behavior similar to that observed with moderate  $h/M$  values in the  $a/M = 0.4$  and  $a/M = 0.6$  models. Conversely, in the  $V_\infty/c = 0.4$  and  $V_\infty/c = 0.6$  models, the oscillation modes of the shock cone are notably distinct, as discussed in detail in Section 5. Specifically, in the case of  $V_\infty/c = 0.6$ , the decrease in the cone opening angle and the stagnation point closer proximity to the black hole horizon lead to the complete disappearance of oscillations in the mass accretion rate, as seen in Fig.12. As a result, no QPO mode is excited for  $V_\infty/c = 0.6$ . Interestingly, in the case of  $V_\infty/c = 0.4$ , only the  $f_{sh}$  mode, which occurs at the stagnation point along the azimuthal direction, is observed.

We examine the influence of the asymptotic speed alongside the scalar hair parameter on the dynamics of the shock cone and the excitation of oscillation modes, uncovering intriguing results. As the absolute value of the scalar hair parameter and the asymptotic speed both increase, the shock cone opening angle and the time required for accreting matter to reach a steady state decrease. Concurrently, the stagnation point moves closer to the black hole horizon in both scenarios. However,

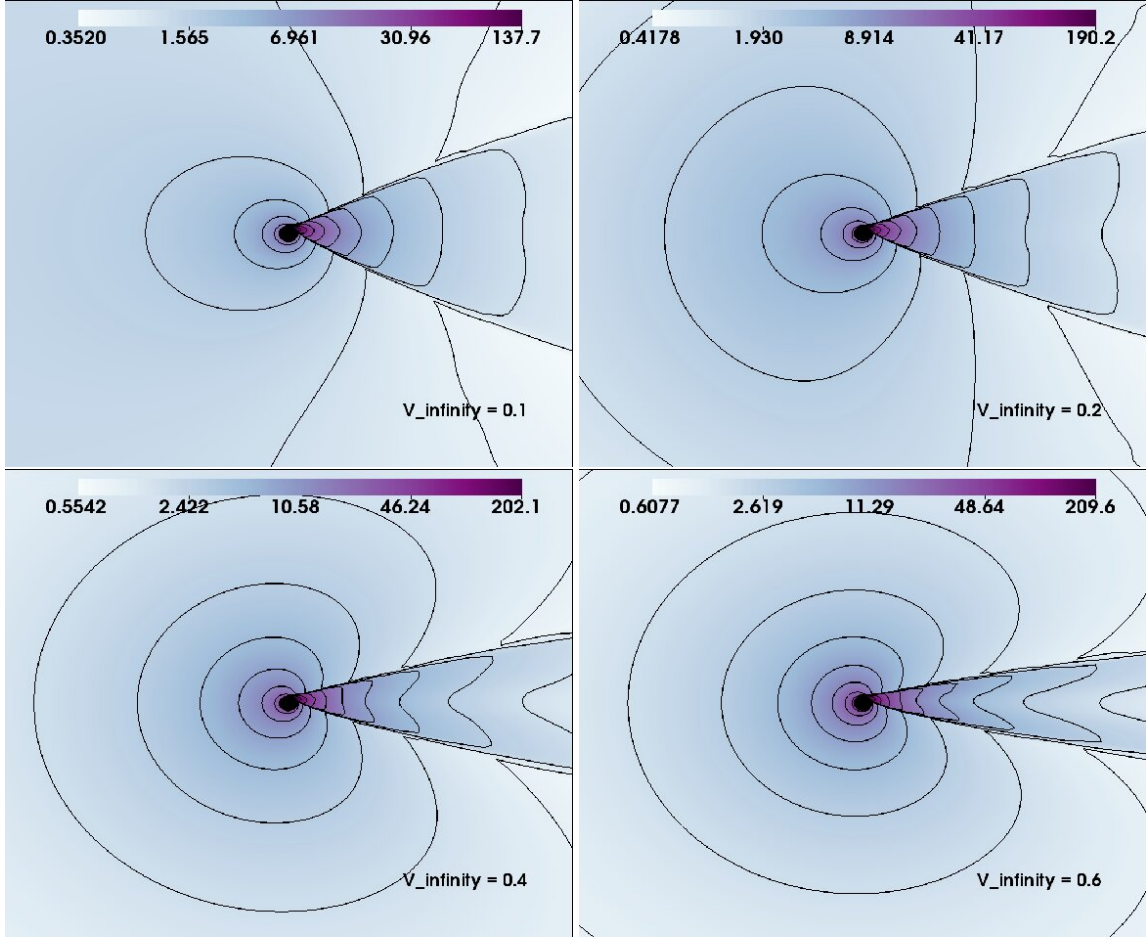


**Figure 11.** Same as in Fig.9 but for the  $a/M = 0.9$  with  $h/M = -0.25$  for various values of asymptotic velocity  $V_\infty/c$  to show the effect of the velocity of the matter injected from outer boundary to the shock cone dynamics. Each snapshot has been plotted at the maximum time of the simulation.

while the rest-mass density of the matter accreted inside the cone decreases with an increase in the absolute value of  $h/M$ , it increases as the asymptotic speed rises. Thus, as the hair parameter grows, the shock cone and QPOs gradually vanish, whereas the cone stability and the oscillation frequencies are enhanced by an increase in the asymptotic speed.

In Fig. 12, we present the variation in the mass accretion rate at different asymptotic speeds for  $a/M = 0.9$  and  $h/M = -0.25$ , along with the Kerr solution at  $V_\infty/c = 0.2$ . At the same asymptotic speed, the Horndeski solution for  $h/M = -0.25$  significantly differs from the Kerr solution. This divergence is evident both in the time it takes for the system to reach the steady state and in the pattern of matter accretion towards the black hole. These differences influence the

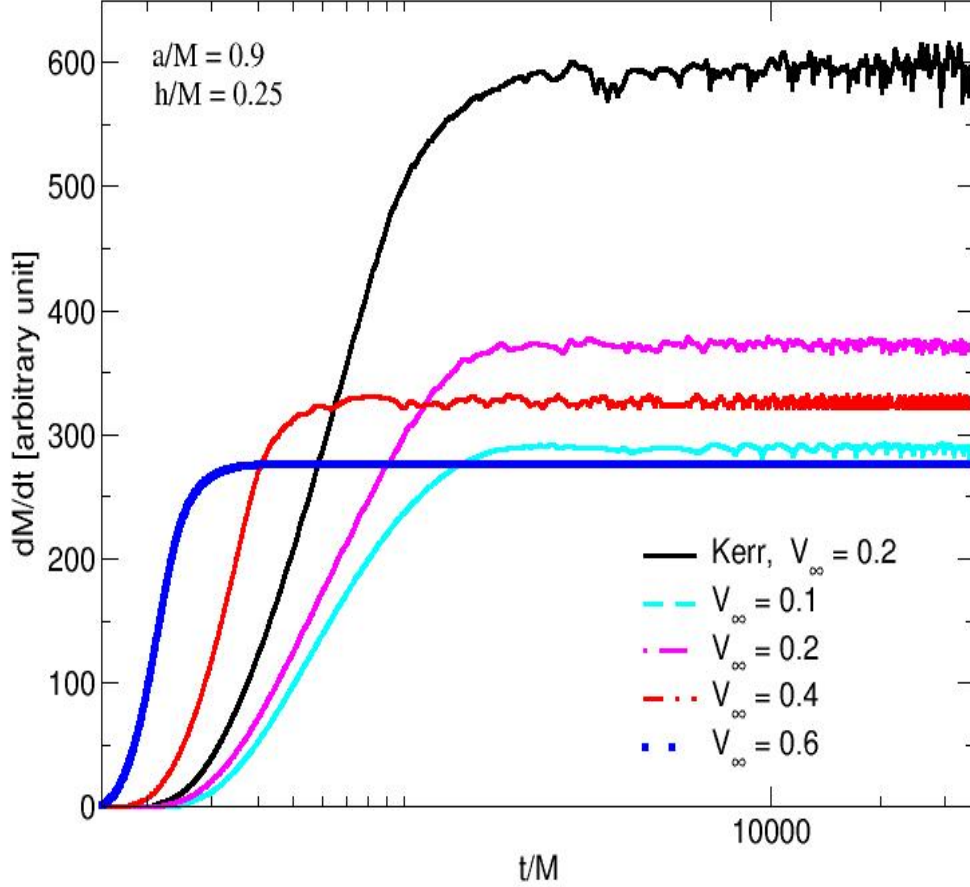


**Figure 12.** Same as in Fig.5 but it is for  $a/M = 0.9$  with  $h/M = -0.25$  for various values of asymptotic velocity  $V_\infty/c$ .

dynamics of the shock cone and the QPOs. Additionally, variations in the asymptotic speed impact the stability and oscillations of the cone. Specifically, at  $V_\infty/c = 0.2$ , the shock cone achieves stability without creating instabilities after reaching the steady state, resulting in the absence of QPO formation in this model.

#### 4.7 The Comparison of $V_\infty/c = 0.4$ from $a/M = 0.9$ with $h/M = -0.25$ and $a/M = 0.6$ with $h/M = -0.8$

To better understand the impact of asymptotic speed, we examine the structure of the shock cone and the resulting QPOs in two black hole models: one with rapid rotation ( $a/M = 0.9$ ) and the other with moderate rotation ( $a/M = 0.6$ ), both at the same asymptotic speeds ( $V_\infty/c = 0.4$ ). We utilize extreme hair parameters in both cases to deepen our understanding of the effects of asymptotic velocity and the hair parameter on the formation of the shock cone in the vicinity of the Horndeski black hole. The following results reveal that the asymptotic speed significantly influences the accretion mechanism, the structure of the shock cone, and the QPOs. Indeed, to fully

comprehend the impact of asymptotic speed on these phenomena, further studies across a wide range of parameters are necessary. Through such research, we anticipate that some observational results could be elucidated.

According to the results obtained from the numerical models with varying rotation and hair parameters, it has been observed that the hair parameter significantly influences the dynamic structure of the formed shock cone and the amount of matter trapped inside the cone. It can even cause the complete disappearance of the shock cone and the trapped modes of QPOs. However, the black hole rotation parameter only alters the value of the excited frequencies, without making a noticeable impact on the other conditions mentioned above. Despite using different rotation parameters, as shown in Fig. 13, it is numerically observed that the rotation parameter does not affect the general physical structure of the cone. However, as seen in Fig. 13 and other models, the scalar hair parameter, which significantly affects the speed of matter falling towards the black hole asymptotically and spacetime, changes the formation of the shock cone.

In Fig. 13, we modeled the dynamic structure of the shock cones in the presence of strong scalar fields for two separate rotation parameters at the same asymptotic speed. According to Fig. 13, an increase in the intensity of the scalar field leads to changes in the stagnation point within the cone and also results in a decrease in the amount of matter trapped inside the cone. This, in turn, has led to the formation of a bow shock in the later stages (see the bottom part of Fig. 13). The bow shock is formed entirely by the matter on the downstream side being pushed towards the upstream side due to the strong scalar field. The same phenomenon is observed in the bottom left graph of Fig. 6. However, in that case, since the asymptotic speed is lower than the one used in Fig. 13, the shock cone has completely disappeared, and the matter has started to be pushed back in the direction from which it came. In other words, we can only identify the formation of a bow shock. But since it is a weak bow shock, no QPO frequencies have been observed in the numerical calculations.

## 5 Possible QPO Models and Observed Frequencies from Numerical Simulations

Understanding the nature of QPOs through alternative theories of gravity [63–66] and an extra spatial dimension [67, 68] could provide valuable insights for explaining some observational data in AGN and microquasar systems that cannot be accounted for by Kerr gravity alone. In this context, we explore the oscillation frequencies trapped by shock cones formed as a result of the BHL accretion around rotating Horndeski black holes. Unlike Kerr black holes, Horndeski black holes possess a scalar hair parameter, prompting us to investigate its effect on QPOs. Within the shock cones, one of the intrinsic modes is the  $p$  mode. The frequencies emerging from the  $p$  mode, formed within the torus and the shock cone around the Kerr black hole, depend on the black hole rotation parameter and the accretion mechanism. However, the frequency of oscillations excited by shock cones around the rotating Horndeski black hole not only depends on these parameters but also undergoes significant changes due to the black hole hair parameter  $h/M$ . This variation is numerically observed in the Power Spectral Density (PSD) analyses for  $a/M = 0.6$  and  $a/M = 0.9$ , as illustrated in Figs. 14 and 15. This behavior is also reported in Ref. [25]. The scalar hair parameter, which defines the scalar field as discussed in Ref. [25], not only modifies existing frequencies but also leads to the creation of new frequencies. A schematic representation of these frequencies is provided in Figure 8 of Ref. [25]. As a consequence of the scalar hair parameter effect, various



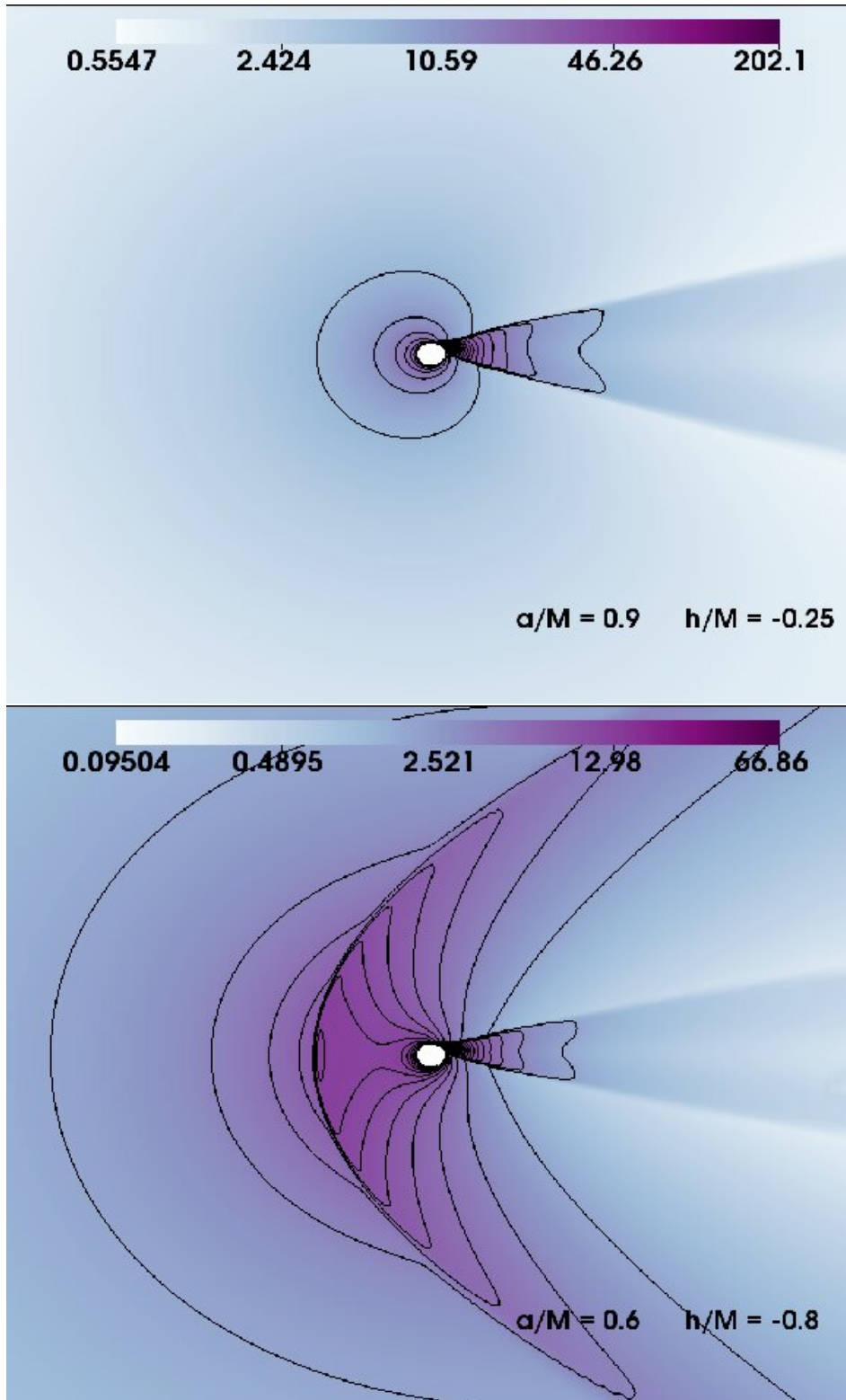


**Figure 13.** Same as in Fig.4 but for  $a/M = 0.9$  with  $h/M = -0.25$  and  $a/M = 0.6$  with  $h/M = -0.8$  with the same asymptotic velocity  $V_\infty/c = 0.4$ . The effect of the  $V_\infty/c$  along with black hole scalar hair parameter is shown.

frequencies have been observed, depending on the parameter. These include the oscillation frequency  $f_{EH}$  between the stagnation point and the black hole horizon at  $r = 2.3M$ , the oscillation frequency  $f_{\phi_{max}}$  between the stagnation point and the point where the scalar field is maximum, the oscillation frequency  $f_{bow}$  of the  $p$  mode trapped along the azimuthal length, and the low-frequency  $p$  mode oscillation  $f_{sh}$ , as detailed in Ref.[25].

Based on the initial conditions given in Table 1, as observed in Figs.4 and 9 through numerical modeling, no bow shock has formed. This reveals the presence of three different fundamental modes, which are  $f_{sh}$ ,  $f_{EH}$ , and  $f_{\phi_{max}}$ , in our numerical simulations. Fig.14 demonstrates the variation of trapped QPO frequencies within the shock cone formed on the downstream side of the rotating Horndeski black hole ( $a/M = 0.6$ ), depending on the Horndeski hair parameter ( $h/M$ ). Each plot compares Horndeski gravity under different  $h/M$  (represented with a red dashed line) with Kerr gravity (represented with a black straight line), revealing how QPO behavior changes with  $h/M$ . It is observed that the frequencies of the resulting QPOs change; the fundamental modes gradually decrease and even fail to form for  $h/M = -0.8$ . This occurs due to the decrease in the cone opening angle and the stagnation point, as calculated in numerical simulations and provided in Table 1. The stagnation point gets closer to the black hole horizon as  $h/M$  increases in the negative direction. The narrowing of the cone opening angle leads to an increase in the  $f_{sh}$  frequency. On the other hand, the stagnation point moving closer to the black hole horizon causes the frequencies of the  $f_{EH}$  and  $f_{\phi_{max}}$  modes to increase and even disappear.

We compare the QPOs for every value of  $h/M$  with the Kerr case. It is observed that while all QPO frequencies occur in Kerr gravity, with different  $h/M$  values, the amplitudes of the same frequencies decrease, they appear at higher frequencies, or completely disappear for some models. For instance, at  $h/M = -0.1$  and  $h/M = -0.2$ , these three fundamental QPO modes are formed. However, at  $h/M = -0.4$ , only two of them are observed, and at  $h/M = -0.6$ , only one is detected. At  $h/M = -0.8$ , these three modes disappear. According to our understanding from numerical observations, the two modes present at  $h/M = -0.4$  are  $f_{sh}$  and  $f_{EH}$ , while the mode at  $h/M = -0.6$  is  $f_{sh}$ . The disappearance of the other modes is attributed to the stagnation point proximity to the black hole. Apart from these modes, the peaks observed across all models result from QPO frequencies generated by nonlinear coupling.  $f_{sh}$ ,  $f_{EH}$ , and  $f_{\phi_{max}}$  interact within themselves, stacking on top of each other to create new QPO oscillation frequencies. These are also used to explain the twin-peak QPOs [33] or ratios such as 1 : 2 : 3... in their interpretation.

Fig. 15 demonstrates the behavior of QPO modes trapped within the shock cone occurring in the downstream region around the Horndeski black hole with a rotation parameter of  $a/M = 0.9$ , as a function of  $h/M$ . As can be seen in Fig. 9 for  $a/M = 0.9$ , the structure of the shock cone formed around the black hole is similar across all  $h/M$  values. The only difference is in the amount of matter trapped within the cone, which decreases as  $h/M$  becomes more negative. The reason for this is summarized in Table 1, regarding the behavior of the stagnation point and the opening angle of the cone. As  $h/M$  increases in the negative direction, the stagnation point moves closer to the black hole horizon. Simultaneously, the cone opening angle decreases. However, since these changes are very small compared to the models with  $a/M = 0.4$  and  $a/M = 0.6$ , the overall structure of the shock cone is preserved. Therefore, it is evident that the shock cone exhibits different behavior from the cases with  $a/M = 0.4$  and  $a/M = 0.6$ .

Due to the preservation of the shock cone general dynamic structure and the stagnation point

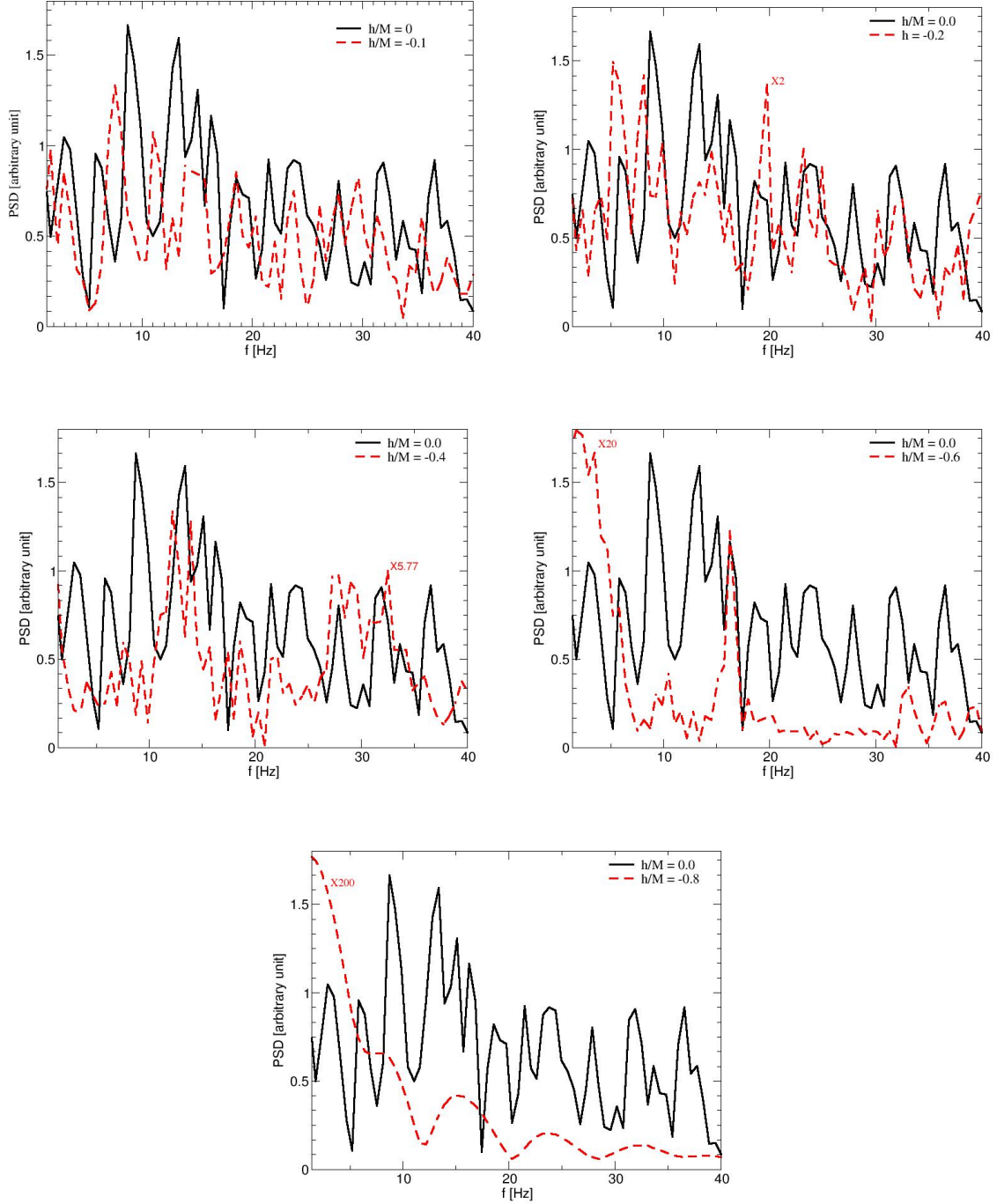


**Figure 14.** The Power Spectral Density (PSD) analysis has been calculated for different values of the hair parameter  $h/M$  for  $a/M = 0.6$ . PSD analysis has been calculated from the mass accretion rate data computed near the black hole horizon. Since the value of  $h/M = 0$  produces the same solution as the Kerr black hole, by comparing the QPO frequencies at different values of  $h/M$  with  $h/M = 0$ , the effect of the scalar hair parameter on the formation of QPOs has been revealed. The mass of the black hole has been chosen as  $M = 10M_{\odot}$ . To directly compare the QPO oscillations in the Kerr case with oscillation frequencies in different hair parameter scenarios, the frequency amplitudes for different hair parameters have been multiplied by certain ratios. These are shown next to the red dashed line in each case.

being sufficiently far from the horizon,  $f_{sh}$ ,  $f_{EH}$ , and  $f_{\phi_{max}}$  have been observed to form within the shock cone for each  $h/M$ . This situation is depicted in Fig.15 alongside the Kerr solution for different  $h/M$  values. As shown in the figure, as  $h/M$  changes, the resulting QPO frequencies occur at higher values, while also displaying differences from the Kerr black hole. As seen in Fig.15, the generated genuine modes lead to the formation of new frequencies through nonlinear couplings. Both these genuine modes and their nonlinear couplings create resonance conditions such as 3 : 2, 5 : 3, 2 : 1, etc. This ratio also represents the lines where the nonlinear couplings occur [69, 70].

As observed across all models of rotating black holes, the scalar hair parameter in Horndeski gravity significantly influences the mass accretion rate, the formation of the shock cone, and the frequencies of QPOs around the black hole. Therefore, the results from our numerical simulations could explain observations that cannot be accounted for by Kerr gravity alone. This underscores the potential importance of alternative theories of gravity, such as Horndeski gravity, in providing explanations for astrophysical phenomena that deviate from the predictions of General Relativity (GR), as modeled by the Kerr metric. The introduction of the scalar hair parameter unveils new dynamics that could help bridge the gap between theory and observations, offering a more comprehensive understanding of the universe most extreme objects.

In addition to the studies mentioned above, in cases where the hair parameter ( $h/M = -0.25$ ) of the rapidly rotating black hole ( $a = 0.9$ ) is close to the critical value, the behavior of the shock cone at different asymptotic speeds reveals that the opening angle of the cone decreases, but the rest-mass density within the cone increases. As shown in Fig.16, this situation significantly impacts the frequencies derived from the numerical simulations. In Fig.16, we examine the frequencies formed at different asymptotic speeds for  $a = 0.9$  and  $h/M = -0.25$ . At  $V_{\infty}/c = 0.1$  and  $V_{\infty}/c = 0.2$ , the frequencies  $f_{sh}$ ,  $f_{EH}$ , and  $f_{\phi_{max}}$ , along with their nonlinear couplings, are visible in the graph below Fig.16. Interestingly, when the opening angle decreases and the stagnation point moves closer to the black hole for  $V_{\infty}/c = 0.4$ , the precise harmonic ratios of 16.82 : 33.89 : 50.96 : 67.41 : 83.98 : 101.06 : 118.13 : 135.34 : 151.84 : 168 : 184.78 : 202.11  $\equiv$  1 : 2 : 3 : 4 : 5 : 6 : 7 : 8 : 9 : 10 : 11 are detected. This might suggest a highly structured and possibly resonant process occurring in the accretion mechanism close to the black hole horizon. From our understanding based on numerical simulation, it is concluded that as the stagnation point approaches very close to the black hole horizon, all radial modes disappear. Only the  $f_{sh}$  mode, which results from the pressure mode, is formed, occurring at 16.8Hz for the black hole with  $M = 10M_{\odot}$ . Then, a series of frequencies produces the aforementioned ratio as a result of the nonlinear coupling of this mode. This situation is clearly shown in the top graph of Fig.16. Moreover, as the stagnation point moves closer to the horizon of the black hole for  $V_{\infty}/c = 0.6$ , no QPO frequency has been observed for  $V_{\infty}/c = 0.6$ , as seen in both Figs.12 and 16. This indicates that, regardless of the shock cone solid structure or its high rest-mass density, if the stagnation point approaches the horizon closer than a certain critical value, it has been observed that no mode is excited within the cone.

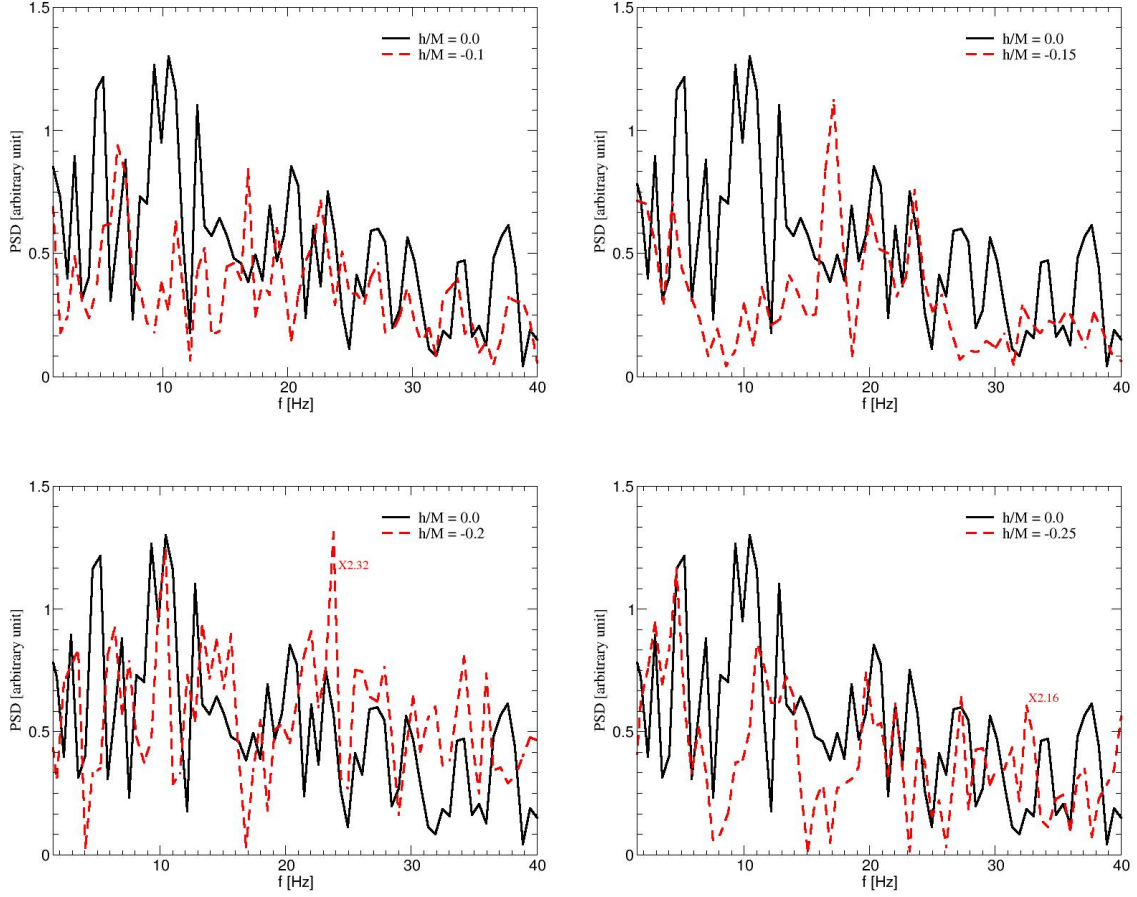
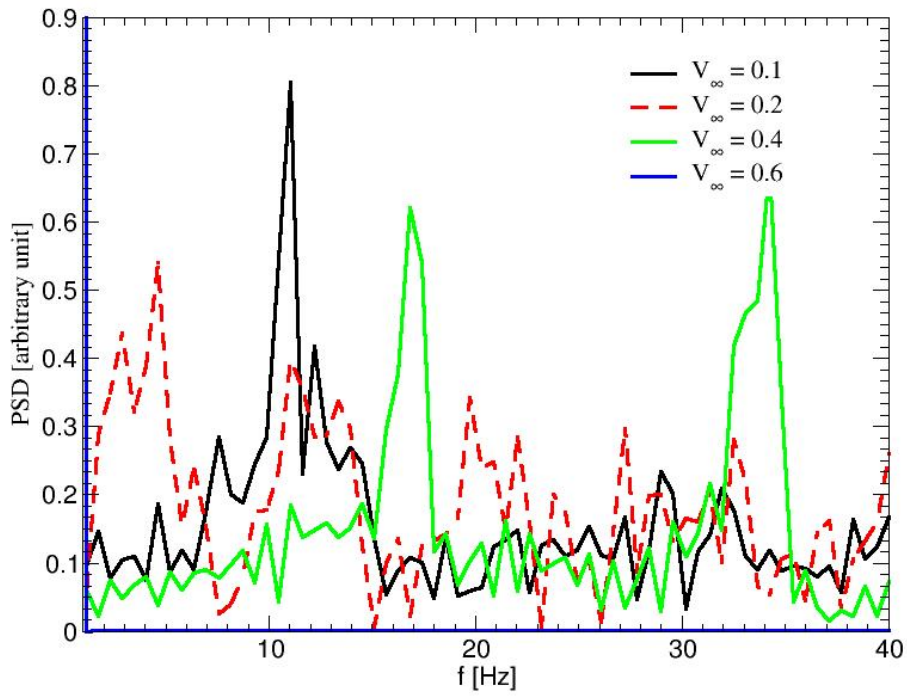
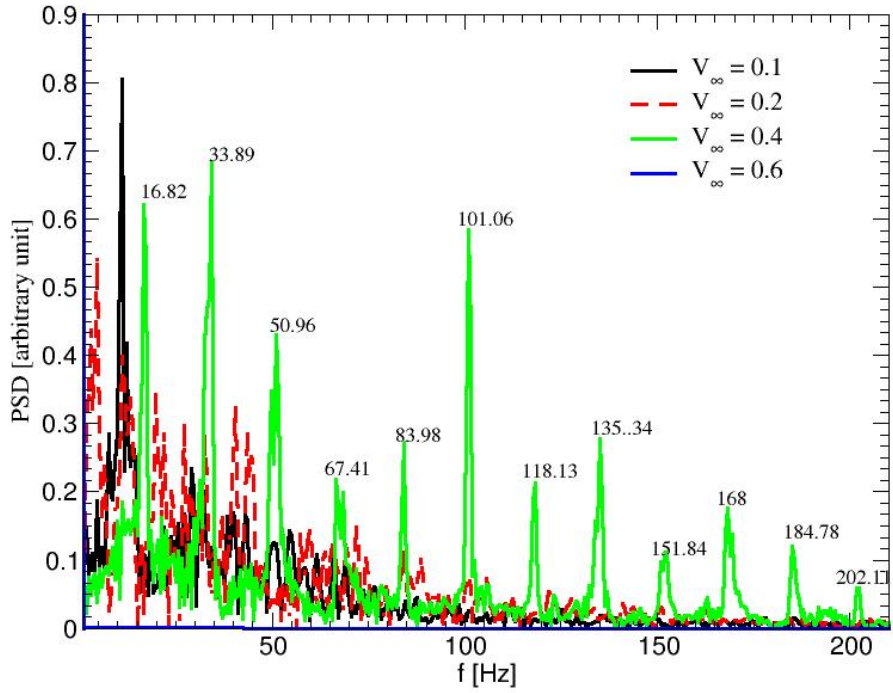


Figure 15. Same as in Fig.14 but it is for  $a/M = 0.9$  models.

## 6 Possible Physical Mechanism and QPOs in M87\*

M87\* is a supermassive black hole located at the center of the NGC 4486 galaxy. It is a black hole whose shadow was directly imaged by the Event Horizon Telescope (EHT) [1–4], with a mass of approximately  $6.5 \times 10^9 M_{\odot}$ . Following the first direct observation, numerous scientists have embarked on studies to further understand the mass, spin parameters, and QPO frequencies of M87\* [71, 72]. Additionally, various attempts have been made to elucidate the physical properties of these black holes and their QPO frequencies using alternative theories of gravity. One such alternative theory is Horndeski gravity. As discussed in detail in this paper, the spacetime around a Horndeski black hole is influenced by both the spin and the scalar hair parameters. It has been theoretically demonstrated that the spacetime experiences significant alterations compared to the Kerr geometry, depending on the hair parameter. Consequently, Ref.[32] analytically applied Horndeski gravity theory to the shadow of M87\* as observed by the EHT, conducting a direct



**Figure 16.** Same as in Fig.14 but it is for  $a/M = 0.9$  with  $h/M = -0.25$  for various values of asymptotic velocity  $V_\infty/c$ . The top graph shows the PSD results for each scenario across a wide frequency range, while the lower one displays changes up to only  $40Hz$ . In the case of the bottom PSD, comparisons at different asymptotic speeds can be made more clearly.

parametric comparison. In their theoretical comparison, they demonstrated that Horndeski gravity could account for the characteristics of M87\*. Assuming M87\* is not a Kerr black hole but a Horndeski black hole, they identified the ranges for the spin and hair parameters of the black hole as  $0.0077 \leq a/M \leq 0.9353$ ,  $-0.756 \leq h/M < 0$  at  $\theta_0 = 90$  (inclination angle), and  $0.0048 \leq a/M \leq 0.9090$ ,  $-0.79 \leq h/M < 0$  at  $\theta_0 = 17$ .

In this paper, we examine the formation of shock cones during BHL accretion around rotating Horndeski black holes, the dynamical behavior of these cones, and the excitation of QPO frequencies within the shock. As detailed in Section 4, we consider cases such as  $a/M = 0.9$  with  $h_c/M = -0.277$ . When  $|h/M| < |h_{max}/M|$ , we model and observe shock cone formation across various models. Given the role of shock cones in exciting QPO modes, we have observed the presence of QPO frequencies for each model at  $a/M = 0.9$ , including genuine modes and their nonlinear couplings. For  $a/M = 0.6$ , with  $h_{max}/M$  at  $-0.983$ , we explore hair parameters for modeling up to  $|h_{max}/M| > |h/M| = 0.8$ . We note the formation of shock cones and QPO frequencies again, with significant changes in the shock cone physical dynamics at  $h/M = -0.6$  and  $h/M = -0.8$ . The change at  $h/M = -0.6$  is less pronounced, allowing the excitation of some modes but not all, resulting in observed QPO frequencies. At  $h/M = -0.8$ , the shock cone structure significantly deforms, nearly reaching the phase of disappearance, leading to no observed QPO frequencies. Lastly, at  $a/M = 0.4$ , with  $h_{max}/M = -1.367$ , the range of  $h/M$  is notably broad. Numerical simulations have shown that at  $|h/M| \geq 0.8$ , the shock cone dynamical structure either changes completely or disappears, preventing the excitation of QPO modes. However, for  $|h/M| < 0.8$ , both the cones and QPO frequencies form.

As a result, the ranges of  $h/M$  and  $a/M$  theoretically defined for M87\*, as outlined in the previous paragraph for different inclination angles, directly align with the values of  $h/M$  necessary for the excitation of shock cones and QPO modes in our numerical models. Thus, we can propose the BHL scenario as the formation mechanism for the shock cone around the M87\* black hole. These shock cones are candidates for a physical mechanism that could excite QPO frequencies, although these frequencies have not yet been observed in this source.

While no specific QPO frequencies have been identified from M87\* observations, both theoretical and numerical models have suggested potential QPO frequencies by describing the space-time fabric around the M87 black hole with a scalar hair parameter from studies.

The QPO frequencies have not yet been detected in observations of M87\*. Theoretical studies [32] have defined the hair parameter for gravity around M87\*. This paper demonstrates, through numerical analysis, that the potential scalar hair parameters for M87\* are consistent with theory. The agreement between theory and numerical simulations suggests that the shock cone physical mechanism proposed here for the M87\* source could be responsible for the potential QPOs observable from this source. Based on these models and corresponding hair parameters, we discuss the possible QPO frequencies that could be observed from the M87\* source.

The PSD analyses in Figs. 14 and 15, recalculated for the mass of the M87\* black hole,  $M = 6.5 \times 10^9 M_\odot$ , reveal that the frequencies resulting from both genuine modes and their nonlinear couplings could occur in the range of  $4.6 \times 10^{-9} - 1.53 \times 10^{-6}$  Hz. As discussed in Chapter 5, the characteristics of the observed frequencies can be said to fall within a certain range, entirely dependent on the hair and black hole spin parameters. It has been observed that as the hair parameter increases in the negative direction, the frequency also increases.

## 7 Understanding the Horndeski parameter-Mass-QPO Relation in GRS 1915 + 105

GRS 1915+105 is one of the well-known  $X$ -ray binaries in our galaxy, exhibiting remarkable  $X$ -ray variability that has drawn significant attention. Analytical and observational studies have shown that the mass of the black hole at the center of this microquasar is approximately  $M \sim 12.5M_{\odot}$ . Observations suggest that the QPO frequencies vary within the range of 1 – 10 Hz [61, 62, 73] and include 34 Hz and 67 Hz in the  $X$ -ray band [74]. It is believed that these oscillations originate from the inner radius of the computational domain [62, 75]. In this section, we attempt to establish the relationship between the mass of the black hole and QPOs with the scalar hair parameter  $h/M$  by comparing our numerical results, which are derived from the mass accretion rate calculated at the inner radius of the computational domain.

When the PSD analysis shown in Figs. 14, 15, and 16 for the black hole GRS 1915+105 is recalculated, it is observed that the frequencies vary between 2.3 Hz and  $f_{nm}$ . Here,  $f_{nm}$  varies depending on the black hole rotation parameter, the asymptotic velocity of the gas in BHL accretion, and the scalar hair parameter  $h/M$ .  $f_{nm}$  could reach up to  $\sim 500$  Hz. When considering  $h/M$ , the observed frequencies of the source occur only when  $|h/M| < 0.25$  for  $a/M = 0.6$  or  $a/M = 0.9$ . If we consider the situation based solely on the asymptotic velocity  $V_{\infty}/c$ , agreement with observations occurs when  $V_{\infty}/c < 0.4$ . On the other hand, for the observational QPOs to be consistent with a scenario where  $|h/M| \geq 0.25$ , or for the asymptotic velocity to be at  $V_{\infty}/c = 0.4$ , the mass of the GRS 1915+105 black hole must be in the range of  $12M_{\odot} \leq M < 400M_{\odot}$ .

## 8 Discussion and Conclusion

We have studied the impact of the scalar field, as defined by Horndeski gravity, on the shock cone formation around rotating black holes. This scalar field, also known as the hair parameter of the Horndeski black hole, modifies the gravitational potential of the spacetime, thereby affecting the mass accretion rate around the black hole. We demonstrate how the hair parameter influences spacetime and, in turn, alters the physical structure of the shock cone resulting from BHL accretion. With changes in the cone structure, we identify conditions under which pressure-based and radial-based QPO frequencies are either excited through nonlinear coupling or completely disappear. These findings underscore the effects of parameters such as the black hole rotation, the scalar field hair parameter, and the asymptotic velocity of the matter injected from the outer boundary.

The scalar hair parameter in Horndeski gravity has different critical values depending on the black hole rotation parameter. In the model of a rapidly spinning black hole with  $a/M = 0.9$ , the numerical results of the shock cones in the vicinity of the Horndeski black hole are similar to the results of Kerr ones because the absolute maximum value of the scalar hair parameter is not very large. Nonetheless, the dynamics of QPO oscillations have been influenced due to the alteration in how spacetime interacts with the scalar potential under varying scalar hair values. As  $h/M$  approaches the critical value, the frequency of the observed fundamental mode has increased. The same situation is also true for slowly rotating black holes. Since the absolute critical hair parameter can take on possibly large values in the slowly rotating black hole cases, the influence of the strong scalar field on the gravitational potential has been stronger. Consequently, as  $h/M$  approaches the critical value, a significant change in the physical structure of the shock cone has been observed.



Also, the opening angle of the shock cone has decreased, the stagnation point has approached closer to the black hole horizon, and the cone has reached the steady state more quickly. At the same time, as more matter within the cone begins to move away from the black hole, the shock cone has started to disappear entirely. Even for  $a/M = 0.4$  with  $h/M = -1.2$ , all the matter in the region of the shock cone is expelled outward due to the potential of the scalar field. Because of these physical changes, not only have the behaviors and frequencies of the QPOs excited within the shock cone changed, but in the case of a strong scalar field, the QPO frequencies have completely disappeared.

In addition to the scalar hair parameter in Horndeski gravity, modeling some special cases for the asymptotic velocity has revealed the effect of this velocity, along with the hair parameter, on the physical structure of the resulting shock cone and on QPOs. In the case of  $V_\infty/c < 0.4$ , it is observed that all modes within the shock cone are excited, including the fundamental oscillation modes and their nonlinear couplings. However, at  $V_\infty/c = 0.4$ , only the  $f_{sh}$  frequency, created due to the pressure mode, is excited, and this frequency has been seen to exhibit a perfect harmonic resonance. For  $V_\infty/c > 0.4$ , no oscillation mode is found. This confirms that the asymptotic velocity, together with the hair parameter, significantly affects both the structure of the resulting shock cone and the excited QPOs. In our future work, we plan to model different values of  $V_\infty/c$  with different rotation and hair parameters, thereby revealing the physical mechanisms that these three different physical parameters can create. Thus, we will be able to uncover the physical mechanisms behind different observational results from X-ray binaries and AGNs.

The effect of the asymptotic speed and the scalar hair parameter on the dynamics of the shock cone and the excitation of oscillation modes is revealed. The investigation uncovers that an increase in both the absolute value of the scalar hair parameter and the asymptotic speed leads to a reduction in the cone opening angle and a shortened duration for the cone to achieve steady-state. However, the stagnation point approaches the black hole horizon in both scenarios. While the rest-mass density of the matter accreted inside the cone diminishes with an increase in the absolute value of  $h/M$ , this density escalates with an increase in the asymptotic speed. Therefore, an increase in the scalar hair parameter in the negative direction can cause the gradual disappearance of the shock cone and QPOs, while the stability of the cone increases with the asymptotic speed, also altering the oscillations.

The formation of shock cones resulting from BHL accretion, depending on the hair parameter, and the excited QPO frequencies within these cones have also been revealed. Numerical results have shown that shock cones occur at certain values of  $h/M$ , especially for models of slowly rotating black holes. These  $h/M$  values are in agreement with the analytical work conducted by Ref. [32] on the observed  $M87^*$  by the Event Horizon Telescope (EHT). Therefore, the shock cones and the QPOs excited within these cones found in our numerical studies could be suggested for the  $M87^*$  source. Additionally, based on observational results from the GRS 1915+105 black hole, the possible scalar hair parameter for this black hole has been defined. It has been determined that  $h/M > -0.25$  and  $V_\infty/c < 0.4$  are required. On the other hand, for the frequencies obtained from observations to occur with other models used in numerical simulations,  $h/M \leq -0.25$  and  $V_\infty/c = 0.4$ . It has been concluded that the mass of the black hole must be  $12M_\odot \leq M \leq 400M_\odot$ .

In summary, the interaction of weak and strong scalar fields with spacetime has revealed changes in the dynamic structure of shock cones formed around stationary rotating Horndeski black holes during BHL accretion and the behavior of QPO frequencies excited within the cone. The nu-

merical results we have obtained here might be used to provide solutions to some observational data that are not explained by Kerr gravity. Simultaneously, they can be employed to address some mysteries of the universe, such as why QPOs are not observed from some sources. For instance, due to their characteristic structures or certain observational difficulties, QPO behaviors have not been fully determined in XTE J1550-564 [76] and GX 339-4 [77, 78]. Our numerical results could offer an explanation for such X-ray systems.

Superradiance is a phenomenon that occurs as a result of the interaction between a black hole and the surrounding matter. Although the GRH equations we use do not include radiation terms, we can still reveal superradiance scenarios [79, 80]. To do this, after forming a shock cone around the black hole and reaching a steady state, the stability of the shock cone can be examined by perturbing one of the parameters such as density, velocity, or scalar field. The response of the shock cone to the perturbation is calculated over time. Changes in the angular momentum transfer of the cone and the parameters defining the cone are numerically observed in the strong gravitational region, allowing us to study the evolution of the gravitational and scalar fields. However, since the main purpose of the paper is to reveal the impact of the Horndeski scalar field on the shock cone and QPOs, these situations will be addressed in future planned studies.

## Acknowledgments

All simulations were performed using the Phoenix High Performance Computing facility at the American University of the Middle East (AUM), Kuwait. We sincerely thank the referee for their significant contributions to improving the paper and for shedding light on a potential future study.

## References

- [1] Event Horizon Telescope Collaboration, K. Akiyama, A. Alberdi, W. Alef, K. Asada, R. Azulay et al., *First M87 Event Horizon Telescope Results. I. The Shadow of the Supermassive Black Hole*, *APJL* **875** (2019) L1 [1906.11238].
- [2] Event Horizon Telescope Collaboration, K. Akiyama, A. Alberdi, W. Alef, K. Asada, R. Azulay et al., *First M87 Event Horizon Telescope Results. II. Array and Instrumentation*, *APJL* **875** (2019) L2 [1906.11239].
- [3] Event Horizon Telescope Collaboration, K. Akiyama, A. Alberdi, W. Alef, K. Asada, R. Azulay et al., *First M87 Event Horizon Telescope Results. III. Data Processing and Calibration*, *APJL* **875** (2019) L3 [1906.11240].
- [4] Event Horizon Telescope Collaboration, K. Akiyama, A. Alberdi, W. Alef, K. Asada, R. Azulay et al., *First M87 Event Horizon Telescope Results. IV. Imaging the Central Supermassive Black Hole*, *APJL* **875** (2019) L4 [1906.11241].
- [5] R.A. Remillard, E.H. Morgan, J.E. McClintock, C.D. Bailyn and J.A. Orosz, *RXTE Observations of 0.1-300 HZ Quasi-periodic Oscillations in the Microquasar GRO J1655-40*, *APJ* **522** (1999) 397.
- [6] S. Naik, P.C. Agrawal, B. Paul, A.R. Rao, S. Seetha and K. Kasturirangan, *Observation of X-ray transient XTE J1748-288 by the Indian X-ray astronomy experiment*, *AAP* **354** (2000) 938.

- [7] L. Zhang, D. Altamirano, V.A. Cúneo, K. Alabarta, T. Enoto, J. Homan et al., *NICER observations reveal that the X-ray transient MAXI J1348-630 is a black hole X-ray binary*, *MNRAS* **499** (2020) 851 [2009.07749].
- [8] A.R. Ingram and S.E. Motta, *A review of quasi-periodic oscillations from black hole X-ray binaries: Observation and theory*, *NAR* **85** (2019) 101524 [2001.08758].
- [9] C.S. Reynolds, *Observing black holes spin*, *Nature Astronomy* **3** (2019) 41 [1903.11704].
- [10] K.L. Smith, C.R. Tandon and R.V. Wagoner, *Confrontation of Observation and Theory: High-frequency QPOs in X-Ray Binaries, Tidal Disruption Events, and Active Galactic Nuclei*, *APJ* **906** (2021) 92 [2011.05346].
- [11] Y.J. Jin, W. Wang, X. Chen, P.F. Tian, Q. Liu, P. Zhang et al., *Quasi-periodic Oscillations in GX 339-4 during the 2021 Outburst Observed with Insight-HXMT*, *APJ* **953** (2023) 33 [2306.13994].
- [12] H. Bondi and F. Hoyle, *On the mechanism of accretion by stars*, *MNRAS* **104** (1944) 273.
- [13] H. Bondi, *On spherically symmetrical accretion*, *MNRAS* **112** (1952) 195.
- [14] R. Edgar, *A review of Bondi-Hoyle-Lyttleton accretion*, *NAR* **48** (2004) 843 [astro-ph/0406166].
- [15] D. Giulini, *Luciano Rezzolla and Olindo Zanotti: Relativistic hydrodynamics. Oxford University Press, Oxford, 2013, 752 pp, GBP 55.00, ISBN: 978-0-19-852890-6, General Relativity and Gravitation* **47** (2015) 3.
- [16] O. Dönmez, O. Zanotti and L. Rezzolla, *On the development of quasi-periodic oscillations in Bondi-Hoyle accretion flows*, *MNRAS* **412** (2011) 1659 [1010.1739].
- [17] A.J. Penner, *General relativistic magnetohydrodynamic Bondi-Hoyle accretion*, *Monthly Notices of the Royal Astronomical Society* **414** (2011) 1467 [https://academic.oup.com/mnras/article-pdf/414/2/1467/3006943/mnras0414-1467.pdf].
- [18] O. Zanotti, C. Roedig, L. Rezzolla and L. Del Zanna, *General relativistic radiation hydrodynamics of accretion flows - I. Bondi-Hoyle accretion*, *MNRAS* **417** (2011) 2899 [1105.5615].
- [19] O. Dönmez, *Relativistic simulation of flip-flop instabilities of Bondi-Hoyle accretion and quasi-periodic oscillations*, *MNRAS* **426** (2012) 1533.
- [20] A.J. Penner, *Ultrarelativistic Bondi-Hoyle accretion – I. Axisymmetry*, *Monthly Notices of the Royal Astronomical Society* **428** (2012) 2171 [https://academic.oup.com/mnras/article-pdf/428/3/2171/3648199/sts176.pdf].
- [21] F.D. Lora-Clavijo and F.S. Guzmán, *Axisymmetric Bondi-Hoyle accretion on to a Schwarzschild black hole: shock cone vibrations*, *MNRAS* **429** (2013) 3144 [1212.2139].
- [22] F. Koyuncu and O. Dönmez, *Numerical simulation of the disk dynamics around the black hole: Bondi-Hoyle accretion*, *Modern Physics Letters A* **29** (2014) 1450115.
- [23] F.D. Lora-Clavijo, A. Cruz-Osorio and E. Moreno Méndez, *Relativistic Bondi-Hoyle-Lyttleton Accretion onto a Rotating Black Hole: Density Gradients*, *APJS* **219** (2015) 30 [1506.08713].
- [24] A. Cruz-Osorio and L. Rezzolla, *Common-envelope Dynamics of a Stellar-mass Black Hole: General Relativistic Simulations*, *APJ* **894** (2020) 147 [2004.13782].
- [25] A. Cruz-Osorio, L. Rezzolla, F.D. Lora-Clavijo, J.A. Font, C. Herdeiro and E. Radu, *Bondi-Hoyle-Lyttleton accretion onto a rotating black hole with ultralight scalar hair*, *JCAP* **2023** (2023) 057 [2301.06564].

- [26] Donmez, Orhan, *Bondi-hoyle accretion around the non-rotating black hole in 4d einstein-gauss-bonnet gravity - bondi-hoyle around egb black hole*, *Eur. Phys. J. C* **81** (2021) 113.
- [27] O. Donmez, *Dynamical evolution of the shock cone around 4D Einstein-Gauss Bonnet rotating black hole*, *Physics Letters B* **827** (2022) 136997 [2103.03160].
- [28] O. Donmez and F. Dogan, *The Shock Cone Instabilities and Quasi-Periodic Oscillations around the Hartle–Thorne Black Hole*, *Universe* **10** (2024) 152.
- [29] G.W. Horndeski, *Second-Order Scalar-Tensor Field Equations in a Four-Dimensional Space*, *International Journal of Theoretical Physics* **10** (1974) 363.
- [30] J. Kumar, S.U. Islam and S.G. Ghosh, *Investigating strong gravitational lensing effects by supermassive black holes with Horndeski gravity*, *European Physical Journal C* **82** (2022) 443 [2109.04450].
- [31] K.-i. Kubota, S. Arai and S. Mukohyama, *Propagation of scalar and tensor gravitational waves in Horndeski theory*, *PRD* **107** (2023) 064002 [2209.00795].
- [32] M. Afrin and S.G. Ghosh, *Testing Horndeski Gravity from EHT Observational Results for Rotating Black Holes*, *APJ* **932** (2022) 51 [2110.05258].
- [33] J. Rayimbaev, K.F. Dialektopoulos, F. Sarikulov and A. Abdujabbarov, *Quasiperiodic oscillations around hairy black holes in Horndeski gravity*, *European Physical Journal C* **83** (2023) 572 [2307.03019].
- [34] X.-J. Gao, T.-T. Sui, X.-X. Zeng, Y.-S. An and Y.-P. Hu, *Investigating shadow images and rings of the charged Horndeski black hole illuminated by various thin accretions*, *European Physical Journal C* **83** (2023) 1052 [2311.11780].
- [35] S.G. Ghosh and M. Afrin, *An Upper Limit on the Charge of the Black Hole Sgr A\* from EHT Observations*, *APJ* **944** (2023) 174 [2206.02488].
- [36] X.-J. Wang, X.-M. Kuang, Y. Meng, B. Wang and J.-P. Wu, *Rings and images of Horndeski hairy black hole illuminated by various thin accretions*, *PRD* **107** (2023) 124052 [2304.10015].
- [37] S. Hu, D. Li, C. Deng, X. Wu and E. Liang, *Influences of tilted thin accretion disks on the optical appearance of hairy black holes in Horndeski gravity*, *arXiv e-prints* (2023) arXiv:2309.10557 [2309.10557].
- [38] M. Heydari-Fard, M. Heydari-Fard and N. Riazi, *Thin accretion disk images of rotating hairy Horndeski black holes*, *arXiv e-prints* (2023) arXiv:2311.12393 [2311.12393].
- [39] J. Magaña and T. Matos, *A brief Review of the Scalar Field Dark Matter model*, in *Journal of Physics Conference Series*, vol. 378 of *Journal of Physics Conference Series*, p. 012012, IOP, Aug., 2012, DOI [1201.6107].
- [40] L.O. Téllez-Tovar, T. Matos and J.A. Vázquez, *Cosmological constraints on the multiscalar field dark matter model*, *PRD* **106** (2022) 123501 [2112.09337].
- [41] G. Gómez and P. Valageas, *Constraining self-interacting scalar field dark matter from the black hole shadow of the Event Horizon Telescope*, *PRD* **109** (2024) 103038 [2403.08988].
- [42] T. Matos, F.S. Guzmán and D. Núñez, *Spherical scalar field halo in galaxies*, *PRD* **62** (2000) 061301 [astro-ph/0003398].
- [43] T. Matos and L.A. Ureña-López, *LETTER TO THE EDITOR: Quintessence and scalar dark matter in the Universe*, *Classical and Quantum Gravity* **17** (2000) L75 [astro-ph/0004332].

- [44] J.A. Font, *Numerical Hydrodynamics in General Relativity*, *Living Reviews in Relativity* **3** (2000) 2 [[gr-qc/0003101](#)].
- [45] O. Dönmez, *Code Development of Three-Dimensional General Relativistic Hydrodynamics with AMR (Adaptive-Mesh Refinement) and Results from Special and General Relativistic Hydrodynamics*, *APSS* **293** (2004) 323 [[gr-qc/0406073](#)].
- [46] O. Donmez, *Solution of the 1D Special Relativistic Hydrodynamics(SRH) Equations Using Different Numerical Method and Results from Different Test Problems*, *AM&C* **181** (2006) 256 [[gr-qc/0512104](#)].
- [47] L.D. Landau and E.M. Lifshitz, *Fluid mechanics* (1959).
- [48] E. Babichev, C. Charmousis and A. Lehébel, *Asymptotically flat black holes in Horndeski theory and beyond*, *JCAP* **2017** (2017) 027 [[1702.01938](#)].
- [49] S. Esteban Perez Bergliaffa, R. Maier and N. de Oliveira Silvano, *Hairy Black Holes from Horndeski Theory*, *arXiv e-prints* (2021) arXiv:2107.07839 [[2107.07839](#)].
- [50] R.K. Walia, S.D. Maharaj and S.G. Ghosh, *Rotating black holes in Horndeski gravity: thermodynamic and gravitational lensing*, *European Physical Journal C* **82** (2022) 547 [[2109.08055](#)].
- [51] M. Azreg-Aïnou, *From static to rotating to conformal static solutions: rotating imperfect fluid wormholes with(out) electric or magnetic field*, *European Physical Journal C* **74** (2014) 2865 [[1401.4292](#)].
- [52] R.P. Kerr, *Gravitational Field of a Spinning Mass as an Example of Algebraically Special Metrics*, *PRL* **11** (1963) 237.
- [53] C.W. Misner, K.S. Thorne and J.A. Wheeler, *Gravitation. Volume I.* (1977).
- [54] O. Dönmez, *On the development of the Papaloizou-Pringle instability of the black hole-torus systems and quasi-periodic oscillations*, *MNRAS* **438** (2014) 846 [[1304.0584](#)].
- [55] O. Donmez, *Perturbing the stable accretion disk in kerr and 4-d einstein-gauss-bonnet gravities: Comprehensive analysis of instabilities and dynamics*, *Research in Astronomy and Astrophysics* (2024) [[2310.13847](#)].
- [56] M. Ruffert, *Three-dimensional Hydrodynamic Bondi-Hoyle Accretion. I. Code Validation and Stationary Accretors*, *APJ* **427** (1994) 342.
- [57] T. Foglizzo, P. Galletti and M. Ruffert, *A fresh look at the unstable simulations of Bondi-Hoyle-Lyttleton accretion*, *AAP* **435** (2005) 397 [[astro-ph/0502168](#)].
- [58] O. Donmez, F. Dogan and T. Sahin, *Study of Asymptotic Velocity in the Bondi–Hoyle Accretion Flows in the Domain of Kerr and 4-D Einstein–Gauss–Bonnet Gravities*, *Universe* **8** (2022) 458 [[2205.14382](#)].
- [59] W. Xu and J.M. Stone, *Bondi-Hoyle-Lyttleton accretion in supergiant X-ray binaries: stability and disc formation*, *MNRAS* **488** (2019) 5162 [[1907.06108](#)].
- [60] O. Donmez, *From Low- to High-Frequency QPOs around the Non-Rotating Hairy Horndeski Black Hole: Microquasar GRS 1915+105*, Submitted (2024) .
- [61] D. Rawat, M. Pahari, J.S. Yadav, P. Jain, R. Misra, K. Bagri et al., *Study of Timing Evolution from Nonvariable to Structured Large-amplitude Variability Transition in GRS 1915 + 105 Using AstroSat*, *APJ* **870** (2019) 4 [[1811.03393](#)].

- [62] R. Misra, D. Rawat, J.S. Yadav and P. Jain, *Identification of QPO Frequency of GRS 1915+105 as the Relativistic Dynamic Frequency of a Truncated Accretion Disk*, *APJL* **889** (2020) L36 [2001.07452].
- [63] A. Maselli, L. Gualtieri, P. Pani, L. Stella and V. Ferrari, *Testing Gravity with Quasi-periodic Oscillations from Accreting Black Holes: The Case of Einstein-Dilaton-Gauss-Bonnet Theory*, *APJ* **801** (2015) 115 [1412.3473].
- [64] A. Maselli, P. Pani, R. Cotesta, L. Gualtieri, V. Ferrari and L. Stella, *Geodesic Models of Quasi-periodic-oscillations as Probes of Quadratic Gravity*, *APJ* **843** (2017) 25 [1703.01472].
- [65] J. Rayimbaev, P. Tadjimuratov, A. Abdujabbarov, B. Ahmedov and M. Khudoyberdieva, *Dynamics of Test Particles and Twin Peaks QPOs around Regular Black Holes in Modified Gravity*, *Galaxies* **9** (2021) 75 [2010.12863].
- [66] J. Rayimbaev, B. Majeed, M. Jamil, K. Jusufi and A. Wang, *Quasiperiodic oscillations, quasinormal modes and shadows of Bardeen-Kiselev Black Holes*, *Physics of the Dark Universe* **35** (2022) 100930 [2202.11509].
- [67] I. Banerjee, S. Chakraborty and S. SenGupta, *Excavating black hole continuum spectrum: Possible signatures of scalar hairs and of higher dimensions*, *PRD* **96** (2017) 084035 [1707.04494].
- [68] I. Banerjee, S. Chakraborty and S. SenGupta, *Looking for extra dimensions in the observed quasi-periodic oscillations of black holes*, *JCAP* **2021** (2021) 037 [2105.06636].
- [69] R. Remillard, M. Munro, J. McClintock and J. Orosz, *Evidence for Harmonic Relationships in the High Frequency QPOs of XTEJ1550-564 and GROJ1655-40*, in *APS April Meeting Abstracts*, APS Meeting Abstracts, p. N17.076, Apr., 2002.
- [70] T. Belloni, M. Méndez and J. Homan, *The distribution of kHz QPO frequencies in bright low mass X-ray binaries*, *AAP* **437** (2005) 209 [astro-ph/0501186].
- [71] B. Bandyopadhyay, *Jet launching of M87*, *Nature Astronomy* **6** (2022) 14.
- [72] Y. Cui, K. Hada, T. Kawashima, M. Kino, W. Lin, Y. Mizuno et al., *Precessing jet nozzle connecting to a spinning black hole in M87*, *NAT* **621** (2023) 711 [2310.09015].
- [73] P. Tian, P. Zhang, W. Wang, P. Wang, X. Sun, J. Liu et al., *Subsecond periodic radio oscillations in a microquasar*, *NAT* **621** (2023) 271 [2307.14015].
- [74] T.M. Belloni and D. Altamirano, *Discovery of a 34 Hz quasi-periodic oscillation in the X-ray emission of GRS 1915+105*, *MNRAS* **432** (2013) 19 [1303.4934].
- [75] J. Chauhan, P. Bharali, A. Lohfink, Y. Abdulghani and E. Davidson, *A spectral study of GRS 1915+105 during its March 2017 NuSTAR observations*, *MNRAS* **527** (2024) 11801.
- [76] K. Rink, I. Caiazzo and J. Heyl, *Testing general relativity using quasi-periodic oscillations from X-ray black holes: XTE J1550-564 and GRO J1655-40*, *MNRAS* **517** (2022) 1389 [2107.06828].
- [77] Z. Zhang, H. Liu, D. Rawat, C. Bambi, R. Misra, P. Wang et al., *Evolution of QPOs in GX 339-4 and EXO 1846-031 with Insight-HXMT and NICER*, *arXiv e-prints* (2023) arXiv:2305.18249 [2305.18249].
- [78] Y. Zhang, M. Méndez, S.E. Motta, A.A. Zdziarski, G. Marcel, F. García et al., *A systematic study of the high-frequency bump in the black-hole low-mass X-ray binary GX 339 - 4*, *MNRAS* **527** (2024) 5638 [2311.12661].
- [79] V. Cardoso, Ó.J. Dias, J.P. Lemos and S. Yoshida, *Publisher's Note: Black-hole bomb and*

*superradiant instabilities* [*Phys. Rev. D* 70, 044039 (2004)], *PRD* **70** (2004) 049903  
[[hep-th/0404096](https://arxiv.org/abs/hep-th/0404096)].

- [80] R. Brito, V. Cardoso and P. Pani, *Superradiance: Energy extraction, black-hole bombs and implications for astrophysics and particle physics*, 2015,  
<https://api.semanticscholar.org/CorpusID:233872830>.